How correlations change the magnetic structure factor of the kagome Hubbard model

Josef Kaufmann,[1,2] Klaus Steiner,[1,3] Richard T. Scalettar,[3] Karsten Held,[1] and Oleg Janson[2]

[1] *Institute for Solid State Physics, TU Wien, 1040 Vienna, Austria*
[2] *Institute for Theoretical Solid State Physics, IFW Dresden, 01069 Dresden, Germany*
[3] *Department of Physics, University of California, Davis, California 95616, USA*

(Dated: July 3, 2021)

The kagome Hubbard model (KHM) is a paradigmatic example of a frustrated two-dimensional model. While its strongly correlated regime, described by a Heisenberg model, is of topical interest due to its enigmatic prospective spin-liquid ground state, the weakly and moderately correlated regimes remain largely unexplored. Motivated by the rapidly growing number of metallic kagome materials (e.g., Mn_3Sn, Fe_3Sn_2, FeSn, $Co_3Sn_2S_2$, $Gd_3Ru_4Al_{12}$), we study the respective regimes of the KHM by means of three complementary numerical methods: the dynamical mean-field theory (DMFT), the dynamical vertex approximation (DΓA), and determinant quantum Monte Carlo (DQMC). In contrast to the archetypal square-lattice, we find no tendencies towards magnetic ordering, as magnetic correlations remain short-range. Nevertheless, the magnetic correlations undergo a remarkable crossover as the system approaches the metal-to-insulator transition. The Mott transition itself does however not affect the magnetic correlations. Our equal-time and dynamical structure factors can be used as a reference for inelastic neutron scattering experiments on the growing family of metallic kagome materials.

I. INTRODUCTION

Electronic correlations are at the origin of a large variety of exotic phases in transition metal oxides and intermetallic compounds [1–3]. Yet, an adequate description of correlated materials remains a long-standing conundrum in condensed matter physics [4]. Pioneering works of Kanamori [5], Hubbard [6], and Gutzwiller [7] enlightened the key role of onsite Coulomb repulsion as the leading source of electronic correlations. The ensuing model, known as the Hubbard model, became a paradigm of correlated materials: it is widely used to rationalize the experimentally observed phenomena such as metal-to-insulator transitions (MIT) [8], the formation of local moments [9] and high-temperature superconductivity [10].

The flip side of such a rich physics and complexity is that a solution of the Hubbard model becomes intractable for physically relevant regimes. Two prominent exceptions are the one-dimensional [11] and the infinitely-dimensional Hubbard models. The latter can be solved within the dynamical mean-field theory (DMFT) [12, 13], a self-consistent mapping of a lattice Hubbard model onto a single-site Anderson impurity model. This mapping is justified by the rapid suppression of nonlocal correlations concomitant with an increase of the spatial dimensionality or the nearest neighbor coordination number [14, 15]. While in infinite dimensions the DMFT offers an exact solution of the Hubbard model [16], it remains a well-justified approximation for realistic three-dimensional models.

The restriction to local correlations may break down in two-dimensional models relevant for various experimental situations, e.g. in high-temperature superconductors [17], ultrathin van der Waals superlattices [18], and oxide heterostructures [19, 20]. Coordination numbers in such systems are typically small, and hence the outcome of an onsite scattering event strongly depends on the configuration of the neighboring sites. A striking example showing the importance of nonlocal correlations is the square-lattice Hubbard model at half-filling, which describes the physics of parent compounds of cuprate high-temperature superconductors. Here, DMFT finds a first-order Mott transition from a metal to a paramagnetic insulator at low temperatures. Nonlocal cor-

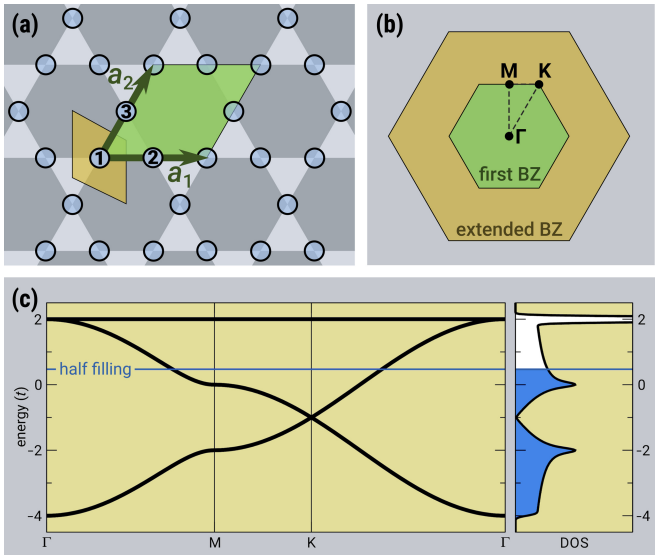

FIG. 1. (a) Unit cell (shaded green) of the kagome lattice described by the basis vectors a_1 and a_2 comprises three sites labeled 1, 2, and 3. The Wigner-Seitz cell is shaded ochre. (b) High-symmetry points of the reciprocal space, the first and the extended Brillouin zones (BZ). (c) The band structure (left) and the density of states (DOS, right) of the tight-binding kagome model with a positive t. The blue line marks the chemical potential $\mu_{\rm tb} \approx 0.47$, for which the non-interacting system is half-filled.

relations drastically change the physics: while short-range antiferromagnetic correlations significantly reduce the critical interaction U, long-range antiferromagnetic correlations shift the MIT to much smaller interactions, even to $U = 0$ for a square lattice Hubbard model with perfect nesting [21, 22]. Long-range antiferromagnetic correlations open a gap. This conclusion is corroborated by quantum Monte Carlo simulations on large finite lattices [21, 23–25]. For two-dimensional lattices without perfect nesting these results suggest a MIT at still considerably lower values of U. As we will see below, for a magnetically frustrated model with only short-range antiferromagnetic correlations, such as the KHM, DMFT only slightly overestimates the critical U of the MIT.

The situation becomes qualitatively different in the presence of frustration. As sizable ground-state degeneracy is typical for a frustrated model, magnetic instabilities may spread over different momenta, suppressing the overall tendency towards magnetic ordering. Ramifications for the MIT are surmised, but model-specific information is scarce. The most studied case, the Hubbard model on the triangular lattice, shows a conventional MIT even if nonlocal correlations are taken into account. However, the triangular lattice has the sizable coordination number of six bonds per site, which is the same as in the 3D cubic lattice. As a result, quantum fluctuations in the triangular lattice are largely suppressed [26, 27].

The kagome lattice (Fig. 1, a) is a much more apt playground to study the interplay of nonlocal correlations and frustration. This simple tessellation of regular hexagons and triangles exhibits a remarkably involved magnetism: the ground state of the $S = \frac{1}{2}$ Heisenberg model on a kagome lattice remains under debate for several decades, with the handful of candidate states comprising a Dirac spin liquid [28–34], a Z_2 spin liquid [35–41], a chiral spin liquid [42–50], and a valence bond solid [51–59]. The vibrant research is boosted by experimental studies of herbertsmithite γ-$Cu_3Zn(OH)_6Cl_2$ [60–62]. This correlated insulator material does not show any sign of magnetic ordering down to lowest temperatures [63], despite the sizable antiferromagnetic exchange of $\sim$200 K [64, 65]. As typical for cuprates, the (screened) onsite Coulomb repulsion U largely exceeds the intersite hopping amplitude t, placing herbertsmithite into the strongly correlated limit of the Hubbard model ($U \gg t$). Interactions between localized $S = \frac{1}{2}$ spins in this limit are well-described by the Heisenberg model.

Much less is known about less correlated regimes of the half-filled kagome Hubbard model (KHM). Dynamical spin correlations were studied using cluster DMFT on a $N = 3$ site clusters [66, 67] where the first-order metal to insulator transition (MIT) occurs at $U_c = 8.4t$ [66]. As was noticed in Ref. [68], a major drawback of odd-numbered clusters is their incompatibility with valence bond states. Instead, variational cluster calculations on $N = 6$ and $N = 12$ clusters demonstrate that the formation of intersite singlets (valence bonds) underlies the MIT, and propels it to a smaller U value. A very recent study suggests that the KHM harbors a topologically nontrivial state, a higher-order topological Mott insulator, characterized by corner modes whose spin excitation spectrum is gapless [69].

For a long time, the KHM attracted little attention: although their potential modifications of herbertsmithite hold promise for unconventional phases [70], pristine herbertsmithite and related quantum magnets [71–73] are correlated insulators deep in the Heisenberg limit, The situation changed drastically after the discovery of metallic kagome materials Mn_3Sn [74–79], Fe_3Sn_2 [80–88], $Co_3Sn_2S_2$ [89–98], $Gd_3Ru_4Al_{12}$ [99, 100], and very recently, FeSn [101–104]. Interestingly, the first three materials exhibit a sizable anomalous Hall effect, associated with a nonvanishing Berry curvature of the occupied bands [75, 83, 89]. While the magnetic moments are associated with the electrons localized in $3d$ or $4f$ shells, neither of the five materials is insulating. Hence, a key to their electronic and magnetic properties should be sought in less correlated regimes of the KHM, which remain hitherto largely unexplored.

In this paper, we fill this gap by performing an extensive numerical investigation of the KHM using three different many-body techniques: the determinant quantum Monte Carlo (DQMC)[105], the dynamical mean-field theory (DMFT) [12, 13], and the dynamical vertex approximation (DΓA) [106, 107]. DQMC is a numerically exact technique for fermionic lattice models. With the caveat that finite lattices beget finite size effects, it provides a sound benchmark for quantum impurity methods. Since frustration of the KHM gives rise to a severe sign problem, we restrict our DQMC calculations to relatively high temperatures. We use these results as a benchmark for DΓA, a diagrammatic extension of DMFT. In contrast to cluster extensions of DMFT [108], this method accounts for nonlocal correlations on all length scales — from short-range to long-range. And unlike many QMC-based techniques, diagrammatic extensions of DMFT are immune to the sign problem [107], allowing us to explore more correlated regimes of the KHM. In this study, we apply the recently implemented self-consistent DΓA scheme [109], which eliminates the need to restore the sum rules by means of so-called λ-corrections [110, 111].

Our main finding is the gradual correlation-induced change in the regime of magnetic correlations: While maxima at the K-point of the extended Brillouin zone are indicative of dominant $\sqrt{3}\times\sqrt{3}$ correlations, the enhancement of interaction strength gives rise to the sign change of third-neighbor correlations. Interestingly, this crossover occurs in the metallic phase, while spin correlations in the moderately correlated regime are similar to those of the Heisenberg model. This finding gives us a key to distinguish between weakly and strongly correlated regimes in the growing family of kagome materials. Furthermore, we compute the dynamical structure factors $S(\mathbf{q}, \omega)$ for the different regimes of the kagome Hubbard model. Since these quantities are accessible in inelastic neutron scattering experiments, the relative strength of

electronic correlations in real materials can be estimated by a direct comparison to our calculated $S(\mathbf{q},\omega)$.

Our study is equally important for method development in the field of electronic correlations: it applies a diagrammatic beyond-DMFT method, DΓA, to a strongly frustrated two-dimensional model. Extensive comparisons with the numerically exact lattice-based method (DQMC) reveal an overall good agreement, indicating that a self-consistent DΓA calculation captures the leading effects of nonlocal fluctuations, even if tendencies towards magnetic ordering are strongly suppressed.

This paper is organized as follows. In Sec. II we introduce the Hubbard model on a kagome lattice, and briefly explain the methods we use to obtain our results. The main results are presented in Sec. III, where we first present the phase diagram and then discuss the magnetic structure factors. In Sec. IV our results are compared to previous theoretical results from the literature and put in the context of present-day experimental research. We summarize our results in Sec. V. Additionally we provide more detailed information about the influence of certain real-space correlations on the structure factor in Appendix .

II. NUMERICAL METHODS

A. KHM Hamiltonian

We define the Hamiltonian of the Hubbard model on a kagome lattice as

$$H = \frac{1}{V_{\mathrm{BZ}}}\int_{\mathrm{BZ}} d\mathbf{k} \sum_{jl,\sigma} h_{jl}(\mathbf{k}) c^{\dagger}_{j\sigma}(\mathbf{k}) c_{l\sigma}(\mathbf{k}) + \sum_{\mathbf{R}}\sum_{j} U n_{\mathbf{R}j\uparrow} n_{\mathbf{R}j\downarrow}, \tag{1}$$

where V_{BZ} is the volume of the Brillouin zone (Fig. 1, b), $\mathbf{k}$ is the 2D crystal momentum, and indices j and l refer to the sites within the unit cell and run from 1 to 3. The three sites comprising the unit cell (as shown in Fig. 1, a) form an equilateral triangle whose side length is a half of the lattice constant. The tight-binding Hamiltonian $h_{jl}(\mathbf{k})$ incorporates the lattice geometry and hopping amplitudes. In the second term, we have a sum over all unit cells, where site $j = 1$ is located at the Bravais lattice position $\mathbf{R}$. The interaction, parametrized by a scalar U, is of density-density type.

As hopping is allowed only between neighbor sites, the non-interacting part of the Hamiltonian reads:

$$h_{jl}(\mathbf{k}) = -t \begin{pmatrix} 0 & 1+e^{ik_1} & 1+e^{ik_2} \\ 1+e^{-ik_1} & 0 & 1+e^{-i(k_1-k_2)} \\ 1+e^{-ik_2} & 1+e^{i(k_1-k_2)} & 0 \end{pmatrix}, \tag{2}$$

where k_1 and k_2 are the projections of $\mathbf{k}$ onto the reciprocal basis vectors $\mathbf{b}_1$ and $\mathbf{b}_2$. We set the hopping amplitude to unity $t \equiv 1$, which defines our unit of energy used throughout the paper. By further setting $\hbar \equiv 1$ and $k_B \equiv 1$ we also fix the units of frequency and temperature.

By applying a unitary transformation $\mathcal{U}(\mathbf{K})$, the Hamiltonian matrix Eq. (2) can be diagonalized

$$h(\mathbf{k}) = \mathcal{U}(\mathbf{k})\, \varepsilon(\mathbf{k}) \mathbb{1}\, \mathcal{U}^{\dagger}(\mathbf{k}), \tag{3}$$

where h and $\mathcal{U}$ are $\mathbf{k}$-dependent matrices of dimension three, $\mathbb{1}$ is a 3×3 identity matrix, and ε is a $\mathbf{k}$-dependent three-dimensional vector, defining the tight-binding bands. The latter are shown in Fig. 1, c. Remarkably, one band is completely flat, corresponding to a δ-peak in the density of states (DOS). The two dispersive bands are identical to those in a honeycomb lattice, featuring two Van Hove singularities and a Dirac crossing. The eigenstates of the flat band correspond to states that are localized on hexagonal plaquettes and combinations thereof [112].

Evaluation of eigenenergies of the full Hubbard Hamiltonian Eq. (1) is not possible: the tight-binding term and the interaction term do not commute. We are therefore restricted to a handful of numerical methods that allow us to calculate correlation functions within a certain approximation. In this work, we use three many-body methods to compute properties of the Hubbard model on a kagome lattice: the dynamical mean-field theory (DMFT), the dynamical vertex approximation (DΓA), and the determinant quantum Monte Carlo (DQMC). Since the kagome lattice is not a standard application of these methods, we briefly review how they work in this case in order to prevent confusion.

B. Dynamical mean-field theory

The dynamical mean-field theory (DMFT) utilizes the equivalence of the Hubbard model in infinite dimensions to an Anderson impurity model. The latter is amenable to an exact numerical evaluation of correlation functions. The pertinent hybridization function of the (auxiliary) Anderson impurity model is determined self-consistently [13]. While DMFT self-energies are frequency-dependent, they lack momentum dependence, i.e., they are local.

Although DMFT workflows are exhaustively described in the literature, we nevertheless provide an outline of our calculation scheme for the sake of clarity. In each step of a DMFT calculation, the four following operations are performed:

1. Calculate the local Green's function $G_{\mathrm{loc}}(i\omega_n)$ for the Hubbard model:

$$G_{\mathrm{loc}}(i\omega_n) = \frac{1}{V_{\mathrm{BZ}}}\int_{\mathrm{BZ}} d\mathbf{k} \Big[\big(i\omega_n + \mu - \Sigma(i\omega_n)\big)\mathbb{1} - h(\mathbf{k}) \Big]^{-1}$$

At this step the chemical potential μ is adapted in order to keep the system half filled. Note that the

local Green's function $G_{\rm loc}(i\omega_n)$ at fermionic Matsubara frequency ω_n is a still a matrix with respect to the three j sites at Bravais lattice site $\mathbf{R}=0$, whereas the self-energy $\Sigma(i\omega_n)$ is scalar multiplied with the 3×3 unit matrix $\mathbb{1}$.

2. Calculate the non-interacting Green's function $\mathcal{G}_j(i\omega_n)$ for the impurity model at site j within the unit cell:

$$[\mathcal{G}_j(i\omega_n)]^{-1} = \Big[\big[G_{\rm loc}(i\omega_n)\big]_{jj}\Big]^{-1} + \Sigma(i\omega_n)$$

This $\mathcal{G}_j(i\omega_n)$ defines three (equivalent) impurity problems for each site j of the unit cell, consistent with the DMFT approximation.

3. Calculate the self-energy $\Sigma(i\omega_n)$ of the impurity models defined in step 2 by an impurity solver. To this end, we use the numerically exact continuous-time quantum Monte Carlo (CT-QMC) algorithm in the hybridization expansion [113]. Since all three impurities are equivalent, we need to do this calculation only once, thus saving computational time.

4. Insert the self-energy $\Sigma(i\omega_n)$ of step 3 into the expression for the Green's function $G_{\rm loc}(i\omega_n)$ in step 1 and iterate until convergence.

Our calculations were carried out by the program package w2dynamics [114]. Although we are solving a three-band model, the downfolding approximation reduces the numerical cost of the DMFT calculation roughly to that of a one-band calculation. By using symmetric improved estimators [115], our DMFT calculations converge very precisely and the resulting self-energies are practically free of noise. Using the final impurity model of the converged DMFT calculation, we compute also the generalized susceptibility in CT-QMC by worm sampling [116].

C. Dynamical vertex approximation (DΓA)

The DΓA [106, 107] is a method based on Feynman diagrams. Compared to DMFT, where the self-energy is local, DΓA goes one step further and imposes locality on the irreducible two-particle vertex. The Bethe-Salpeter equation combines these local building blocks by nonlocal propagator lines and leads to a momentum dependence in the susceptibility. A momentum-dependent self-energy is then obtained via the Schwinger-Dyson equation of motion. In our calculations we use ladder-DΓA, where nonlocal fluctuations are considered only in the density (charge) and the magnetic (spin) channel. In the following, we sketch the DΓA procedure in a compact tensor notation suppressing the frequency and for the lattice quantities momentum and three basis site indices: the interested reader will find a more detailed description in [117] and particularly in [109].

The main input of a DΓA calculation is, besides the tight-binding Hamiltonian, the irreducible vertex $\Gamma_d(\Gamma_m)$ in the density (magnetic) channel. It is computed from the generalized susceptibility χ of the DMFT impurity by the Bethe-Salpeter equation

$$\Gamma_r = \beta^2\big(\chi_r^{-1} - \chi_0^{-1}\big), \tag{4}$$

where r denotes the channel. Note that the inversion is done only with respect to fermionic Matsubara frequencies, since the impurity problem has no orbital degrees of freedom. Next, we perform the following iterative procedure [109]:

1. Calculate momentum-dependent reducible vertices F_d and F_m for the kagome lattice by the Bethe-Salpeter equation

$$F_r = \big[\mathbb{1} - \frac{1}{\beta}\Gamma_r GG\big]^{-1}\Gamma_r \text{ with } r = d \text{ or } m. \tag{5}$$

Here, the inversions pertain also to the site indices j and l, since G is the Green's function of the Hubbard model and thus a 3×3 matrix.

2. Combine F_d and F_m to a crossing symmetric vertex $\mathbf{F}$ as explained in Ref. [117].

3. Compute the momentum-dependent self-energy by the equation of motion, which schematically reads

$$\Sigma(\mathbf{k}) = \frac{1}{2}Un + \frac{1}{\beta^2}UGG\mathbf{F}G. \tag{6}$$

The first term is the static (Hartree) contribution, the second one contains the diagrams of higher order.

4. Construct a new lattice Green's function G by

$$G(\mathbf{k}, i\omega_n) = \Big[(i\omega_n+\mu)\mathbb{1} - h(\mathbf{k}) - \Sigma(\mathbf{k}, i\omega_n)\Big]^{-1} \tag{7}$$

Similar to DMFT, the chemical potential μ can be (slightly) adapted in order to keep the system half filled. This Green's function is now used as a propagator in step 1 and the steps are repeated until convergence in Σ.

After convergence is reached, we obtain the self-energy $\Sigma(\mathbf{k}, i\omega_n)$, which is a full 3×3 matrix in the space of the three lattice sites of our basis and depends, in addition to the fermionic Matsubara frequency, also on the crystal momentum $\mathbf{k}$. A similar procedure for unit cells with multiple equivalent one-orbital impurities was also proposed for the dual fermion approach [118].

D. Determinant quantum Monte Carlo (DQMC)

Mapping onto an auxiliary impurity problem lies at the core of both DMFT and DΓA approaches. It is therefore

crucial to cross-check the DMFT/DΓA results with an independent numerically exact method working explicitly with a *lattice* problem. To this end, we employ determinant quantum Monte Carlo (DQMC) simulations [105]. This technique explicitly computes nonlocal correlation functions, such as the lattice Green's function. Therefore, the main approximation lies in the restriction to a finite cluster. As a consequence, quantities such as the susceptibility or equal time structure factor, which sample correlations to large distance, have corrections which scale as $1/L$, where L is the linear lattice size. However, local (e.g. near neighbor) correlation functions are usually converged to a few percent on lattices of linear extent $L \sim 10$. In the present case computations were done for clusters of 5×5 unit cells (i. e. 75 sites). DQMC calculations also have 'Trotter' errors proportional to the square of the discretization interval of the inverse temperature $\beta = 1/T$. In our work Trotter errors are of the same order as, or smaller than, the statistical errors from the Monte Carlo sampling. Finally, as noted earlier, DQMC calculations are limited by the sign problem [119, 120]. A rough rule of thumb is that DQMC can be done down to temperatures $T \sim W/30$, where W is the bandwidth, for interaction strengths $U \sim W$.

III. RESULTS

We divide our results in two parts. In Sec. III A, we focus on the phase diagram of the KHM in the metallic regime and discuss how the spectral function evolves as a function of the interaction strength and temperature. While it is a common way to describe the physics of a model, we surmise that from the experimental viewpoint such a discussion is largely disconnected from the physics of kagome materials: there is no recipe to extract the information on the interaction strength U for a given material. To alleviate this problem, we present our results for the equal-time $S(\mathbf{q})$ as well as dynamical $S(\mathbf{q}, \omega)$ structure factors for different U values in Sec. III B. As these quantities are experimentally accessible, a direct comparison between theory and experiment can yield an estimate for U.

A. Phase diagram of the kagome Hubbard model

The Hubbard model is famous for exhibiting a transition between a metallic state and an insulating state upon variation of the interaction strength. This generic trend holds for the kagome lattice: In the KHM, the local spectral functions [121] (Fig. 2) show a reduction of the spectral weight around the Fermi level (at $\omega = 0$) upon increasing U, and the system eventually turns insulating once the interaction exceeds a certain critical value U_c. In the high-temperature regime ($T = 0.33$), some spectral weight remains in the gap, but the spectral function develops a distinct dip at the Fermi level, with $U_c \approx 7$ in DQMC and $U_c \approx 9$ in DMFT.

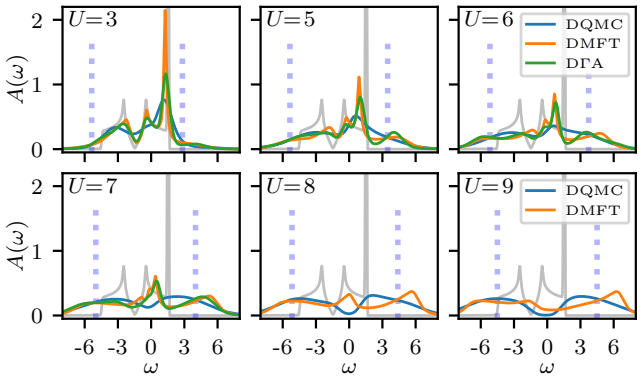

FIG. 2. Local spectral functions for interaction strength ranging from $U = 3$ to 9 at $T = 0.33$ in units of the hopping $t \equiv 1$ as obtained by DMFT, DQMC, and DΓA. The gray line is the density of states of the underlying tight-binding model, the opaque dotted blue bars show the approximate position of the Hubbard bands calculated by Eq. (9).

The transition also manifests itself in the DMFT quasiparticle renormalization factor Z defined as

$$Z = \left[1 - \mathrm{Re}\frac{d\Sigma(\omega)}{d\omega}\Big|_{\omega=0}\right]^{-1}, \tag{8}$$

which decreases from unity in the non-interacting case to zero at the transition to the insulating state. In Fig. 3, we illustrate this behavior for two different temperatures $T = 0.33$ and $T = 0.1$. For the latter, Z vanishes around $U_c \approx 9.45$. At the higher temperature, the critical U is reduced, but its precise estimation is impeded due to thermal broadening. In the same plot, we plot a rough estimate for Z from DQMC, which are estimated as the fraction of the spectral weight located in the quasiparticle region. The latter is determined from the DMFT spectral function for the same U value. For DΓA we calculate a momentum-dependent Z which is presented in Fig. 5 below.

Another characteristic correlation-induced phenomenon is the formation of the Hubbard bands — two incoherent spectral features separated by $\sim U$. As these bands are strongly asymmetric, we estimate their position by

$$\omega_{\mathrm{upper/lower}} = Z_{\mathrm{DMFT}} \times \omega_{\mathrm{max/min}} \pm \frac{U}{2} \tag{9}$$

where $\omega_{\mathrm{max/min}}$ are the upper/lower band edge of the tight binding Hamiltonian, i. e. $2-\mu_{\mathrm{tb}}$ and $-4-\mu_{\mathrm{tb}}$. This heuristic formula interpolates between the non-interacting regime and the strongly correlated insulting regime where the Hubbard bands are at $\pm\frac{U}{2}$. It accounts for the fact that the separation of the Hubbard bands is more than $\pm U$ at small U, and describes the position of the Hubbard bands in Fig. 2 very well.

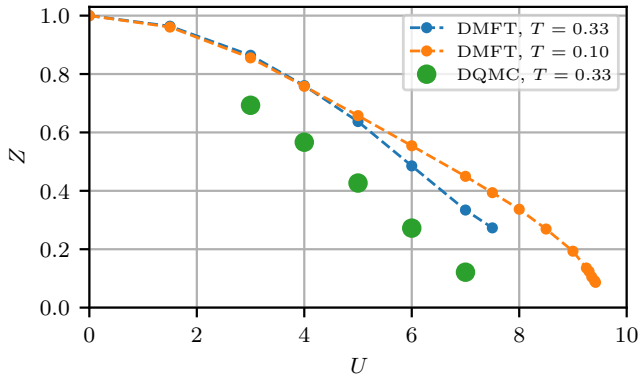

FIG. 3. Quasiparticle renormalization factor Z [Eq. 8] based on DMFT and DQMC data as a function of the interaction strength U for the temperatures specified in the legend box.

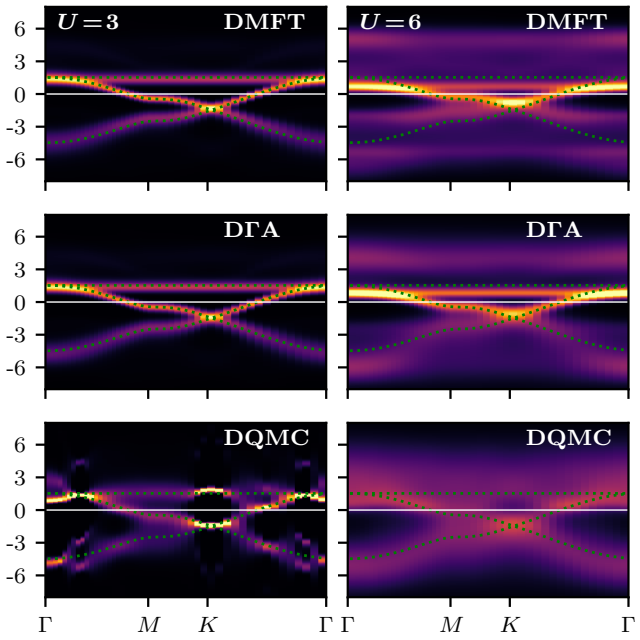

FIG. 4. Spectral functions of DMFT, DΓA and DQMC on a high-symmetry path through the Brillouin zone. The dotted green lines are the tight-binding bands. At weak interaction (left column) there is no sizable renormalization, whereas strong interactions considerably change the spectrum (right column).

Next, we discuss the momentum-resolved spectral functions in the top panels of Fig. 4. In DMFT, they show a textbook behavior, with a renormalized tight-binding band structure and distinct Hubbard bands. Nonlocal correlations alter this picture: the bottom edge of the quasiparticle band merges with the lower Hubbard band at larger interactions, as can be clearly seen in DΓA (Fig. 4, middle panels), and it is even more prominent in DQMC (Fig. 4, bottom panels). More pronounced in DΓA spectrum is a waterfall-like structure between the Γ-point and M/K in the lowest-lying band below the Fermi energy. Such waterfalls have been observed experimentally in angular resolved photoemission spectra (ARPES) of cuprate superconductors [122].

We can extract more insights by comparing the DMFT and DΓA self-energies. In DMFT, the self-energy is diagonal with respect to the three basis-lattice sites j; all three diagonal elements are even identical and there is no off-site contribution within DMFT. In DΓA, the diagonal elements are almost identical to the DMFT self-energy and show only a weak dependence on the momentum. The main difference is the presence of sizable off-diagonal elements that are strongly momentum-dependent.

Analysis of matrix-valued quantities computed on the Matsubara axis is not straightforward. In the case of the KHM, however, we find that the DΓA self-energy commutes with the tight-binding Hamiltonian of Eq. (2):

$$\big[\Sigma(\mathbf{k}, i\omega_n), h(\mathbf{k})\big] = 0. \tag{10}$$

For DMFT this is fulfilled trivially, as Σ is $\mathbf{k}$-independent and proportional to the 3×3 unit matrix for the three sites of the unit cell. In DQMC we do not have direct access to the self-energy, but from the fact that the lattice Green's function approximately commutes with the tight-binding Hamiltonian, we can conclude that this holds for the self-energy as well. This commutation relation implies that the tight-binding bands are mapped onto interacting quasiparticle bands with associated Hubbard bands, but they are not mixed by nonlocal correlations, because the interaction is local. The momentum dependence entails that the self-energy in the band basis is, albeit diagonal, no longer proportional to the unit matrix as in the DMFT. This leads to a momentum- and band-dependent, but still well-defined, quasiparticle renormalization factor $Z_\alpha(\mathbf{k})$, where α is the band index. We show this quantity for $U = 6$ and $T = 1/3$ in Fig. 5. Since smaller Z implies stronger renormalization, it explains why the lowest-lying quasiparticle band merges with the lower Hubbard band at Γ, the center of the Brillouin zone.

Let us compare these results with the well-studied Hubbard model on a square lattice. There, antiferromagnetic fluctuations dominate the phase diagram at all temperatures, leading to an insulating antiferromagnetic state even at smallest values of the interaction U [21] in the limit of zero temperature. Looking at the magnetic susceptibility of the kagome lattice, we have to keep in mind that it is defined as

$$\chi^{jl}_m(\mathbf{q}, i\omega_n) = \sum_{\mathbf{R}} e^{i\mathbf{q}\cdot\mathbf{R}} \int_0^\beta d\tau\, e^{i\omega_n\tau} \langle S^j_z(\mathbf{R}, \tau) S^l_z(\mathbf{0}, 0)\rangle, \tag{11}$$

i.e. it is a 3×3 matrix for each momentum and frequency. For numerical and technical reasons our DΓA calculations are restricted to $\langle S^j_z S^l_z\rangle$ correlation functions, which yield the standard magnetic susceptibility. Note that in the absence of magnetic field, diagonal correlations are

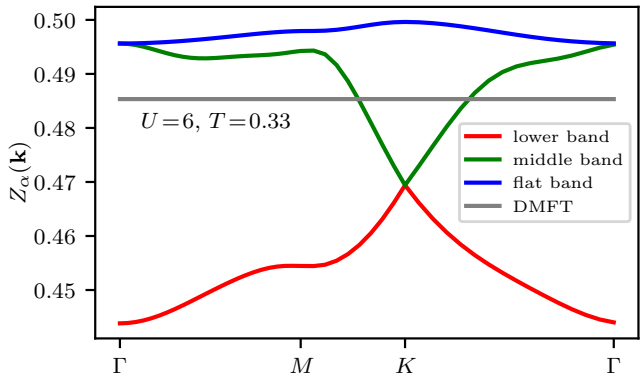

FIG. 5. Momentum- and band-resolved quasiparticle renormalization $Z_\alpha(\mathbf{k})$ at $U = 6$ and $T = 0.33$ obtained by projection of the DΓA self-energy onto the tight-binding eigenbasis.

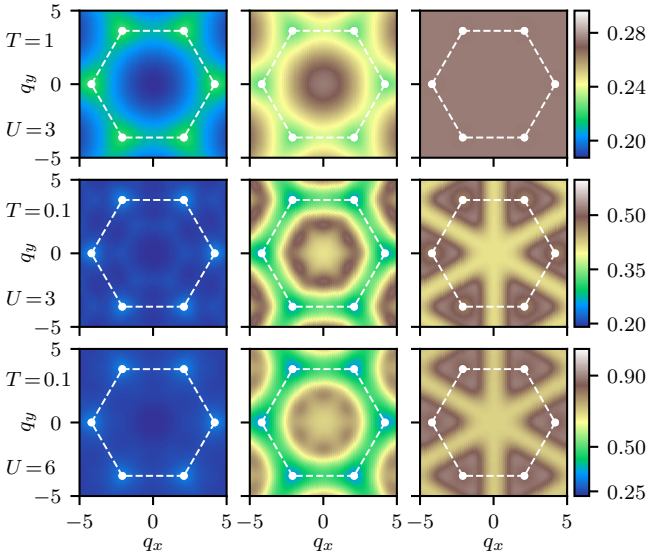

FIG. 6. Eigenvalues of the static magnetic susceptibility in the first BZ for $U = 3$ at $T = 1$ (upper row) and $T = 0.1$ (middle row), and $U = 6$, $T = 0.1$ (lower row). There are three eigenvalues corresponding to the three bands in Fig. 1 (c): the left column shows the projection of χ on the lowest-energy eigenstate [energies below the Dirac point in Fig. 1 (c)]; the middle column that of the part of the bandstructure above the Dirac point and below the flat band; finally the right column corresponds to the flat-band states.

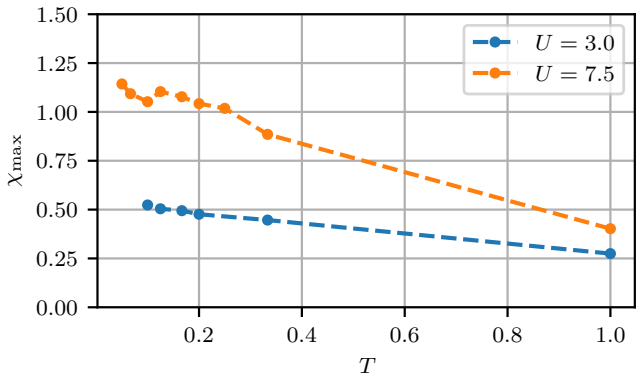

FIG. 7. Temperature dependence of the maximal magnetic susceptibility $\chi_{\max}$ with respect to the momenta and the three eigenvectors (three panels in Fig. 6) at $\omega = 0$ for the weakly ($U = 3$) and moderately ($U = 7.5$) correlated regimes.

equal to one-third of full correlations: $\langle S_z^j S_z^l \rangle = \frac{1}{3}\langle \mathbf{S}^j \cdot \mathbf{S}^l \rangle$. Without symmetry breaking, and as we will see below there are no signs of any long range order, spin-off diagonal correlation functions such as $\langle S_z^j S_x^l \rangle$ or $\langle S_z^j S_+^l \rangle$ vanish [123].

For a quantitative analysis, we resort to the eigenvalues of χ_m^{jl}. Since the susceptibility matrix commutes with the tight-binding Hamiltonian of Eq. (2),

$$\left[\chi_m(\mathbf{k}, i\omega_n), h(\mathbf{k})\right] = 0, \tag{12}$$

we can obtain the three eigenvalues by a projection onto the eigenbasis of the tight-binding Hamiltonian and thus associate the eigenvalues with the respective tight-binding bands. In Fig. 6 we show the (projected) eigenvalues of the zeroth Matsubara frequency on the $\mathbf{q}$-plane for $U = 3$ at high and low temperature.

Notably, the projection of the susceptibility on flat-band eigenstates is also flat at high temperature, but develops an inconspicuous structure at lower temperatures. Most importantly, Fig. 7 reveals that the maximal value of the susceptibility does not increase significantly as the temperature is lowered. Therefore, in sharp contrast to the square lattice, there is no visible tendency towards magnetic ordering. Instead, the flat structure of the magnetic susceptibility indicates short-ranged spin fluctuations.

B. Structure factors

Structure factors are on the one hand inherently connected with magnetic susceptibilities, and on the other hand can be addressed experimentally e.g. by neutron spectroscopy. Following work on the Heisenberg kagome model [124, 125], we calculate the equal-time structure factor $S_0(\mathbf{q})$ given by

$$S_0(\mathbf{q}) = \sum_{j,l} e^{i\mathbf{q}\cdot(\mathbf{r}_j - \mathbf{r}_l)} \sum_{\omega_n} \chi_{jl}(\mathbf{q}, i\omega_n) \tag{13}$$

and the dynamical structure factor $S(\mathbf{q}, \omega)$ given by

$$S(\mathbf{q}, \omega) = \frac{-\mathrm{Im} \sum_{j,l} e^{i\mathbf{q}\cdot(\mathbf{r}_j - \mathbf{r}_l)} \chi_{jl}(\mathbf{q}, \omega + i0^+)/\pi}{1 - e^{-\beta\omega}}. \tag{14}$$

In Eqs. (13) and (14), $\mathbf{r}_j$ denotes the position of the j-th atom in the unit cell. Since the shortest distance between two sites ($\frac{1}{2}$) is twice smaller than the unit cell constant (1), the structure factor is periodic in the extended Brillouin zone (Fig. 1, b). The analytic continuation of Matsubara frequencies or imaginary time to real frequencies

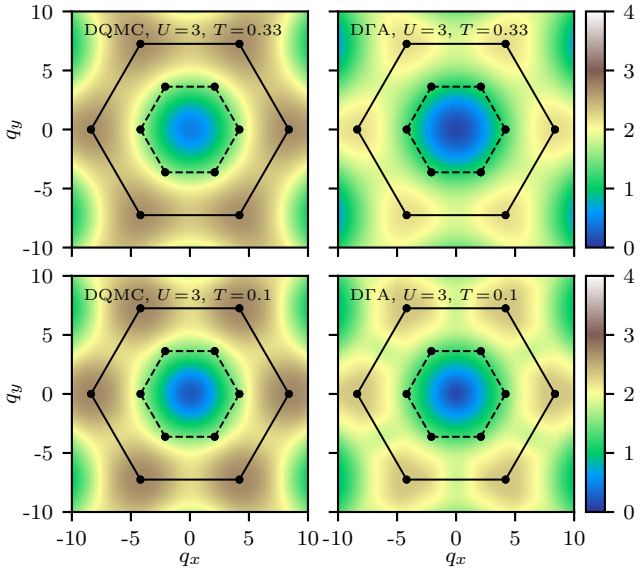

FIG. 8. Equal-time structure factors $S_0(\mathbf{q})$ [Eq. (13)] in the weakly correlated regime ($U = 3$) as a function of temperature (top: $T = 0.33$, bottom: $T = 0.1$). Left: DQMC, right: DΓA. The dashed (solid) hexagons denote the boundary of the (extended) Brillouin zones.

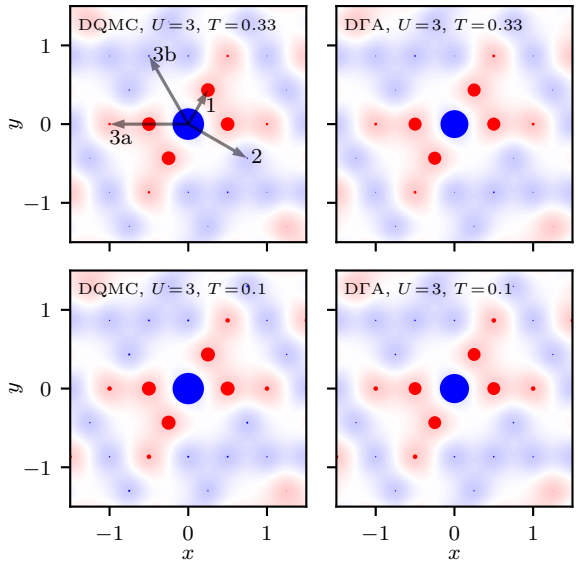

FIG. 9. Equal-time susceptibility $\chi(\mathbf{R} \equiv (x, y))$ in real space for the weakly correlated regime ($U = 3$). Units along the x and y axes are unit cell constants. The area of a circle reflects the absolute value of the respective term, blue color denotes positive (ferromagnetic) correlations, red color denotes negative (antiferromagnetic) correlations. Since the magnitude of the long-range correlations is very small, we add a background shading to indicate the sign. Note that weak long-range correlations are antiferromagnetic for $\mathbf{R}_{3a}$ and ferromagnetic for $\mathbf{R}_2$ and $\mathbf{R}_{3b}$ (see Table I for the notation of intersite vectors).

is performed using ana_cont [126, 127] employing the maximum entropy method [128]. As a technical remark, we note that in DΓA we can analytically continue the projected eigenvalues of the susceptibility matrix individually, and then go back to the sublattice space, where the summation in Eq. (14) is carried out. In the following we present our results for the extended BZ of Fig. 1 (b). Upfolding the three eigenvectors of the first BZ (e.g. for the magnetic susceptibility in Fig. 6) yields a single eigenvector for the larger (extended) BZ.

Fig. 8 shows a smooth distribution of the equal-time structure factor over the extended Brillouin zone, and a weak temperature dependence. In all plots, $S_0(\mathbf{q})$ grows as we move from the center towards the boundary of the extended Brillouin zone, and forms round maxima at its corners [the K-points in Fig. 1 (b)]. To get a deeper insight into magnetic correlations, we return to real space and plot the equal-time susceptibility χ as a function of real-space vector $\mathbf{R}$ connecting two sites. As expected for a strongly frustrated model, the resulting pattern in Fig. 9 is dominated by two contributions: the on-site contribution, which is trivially positive and yields a momentum-independent shift, and sizable negative, i. e. antiferromagnetic, correlations between the nearest neighbors ($\mathbf{R} = \mathbf{R}_1$). As we show in Appendix , the latter are largely responsible for the maxima at the K-points.

More intriguing is the pattern formed by weak longer-range correlations. In particular, by doubling the four $\mathbf{R}_1$, we obtain the $\mathbf{R}_{3a}$ vectors (Table I) that point to four (out of six) third-neighbors on the kagome lattice. A key observation is that the respective correlations are also antiferromagnetic (red circles in Fig. 9). In contrast, the second-neighbor correlations ($\mathbf{R}_2$) and the remaining two third-neighbor correlations ($\mathbf{R}_{3b}$) are ferromagnetic (blue circles in Fig. 9). In momentum space, shown in Fig. 8 this has the following effect: strong negative correlations at $\mathbf{R}_1$ create the peaks at the K-points and positive correlations at $\mathbf{R}_2$ further increase them. The negative correlations at $\mathbf{R}_{3a}$ overcompensate the positive ones at $\mathbf{R}_{3b}$ and thus reduce the structure factor at the M-points. Altogether this leads to well-separated peaks

TABLE I. Four shortest vectors $\mathbf{R}$ in the kagome lattice, connecting nearest neighbors ($\mathbf{R}_1$), second-neighbors ($\mathbf{R}_2$), and third-neighbors ($\mathbf{R}_{3a}$) and ($\mathbf{R}_{3b}$). Vector components and distances are given in units of the lattice constant. (For a visualization of these vectors, see Fig. 9.)

notation	$\lvert\mathbf{R}\rvert$	multiplicity	$\mathbf{R} \equiv (R_x, R_y)$
$\mathbf{R}_1$	$\frac{1}{2}$	4	$\pm\left(\frac{1}{2}; 0\right), \pm\left(\frac{1}{4}; \frac{\sqrt{3}}{4}\right)$
$\mathbf{R}_2$	$\frac{\sqrt{3}}{2}$	4	$\pm\left(0; \frac{\sqrt{3}}{2}\right), \pm\left(-\frac{3}{4}; \frac{\sqrt{3}}{4}\right)$
$\mathbf{R}_{3a}$	1	4	$\pm(1; 0), \pm\left(\frac{1}{2}; \frac{\sqrt{3}}{2}\right)$
$\mathbf{R}_{3b}$	1	2	$\pm\left(-\frac{1}{2}; \frac{\sqrt{3}}{2}\right)$

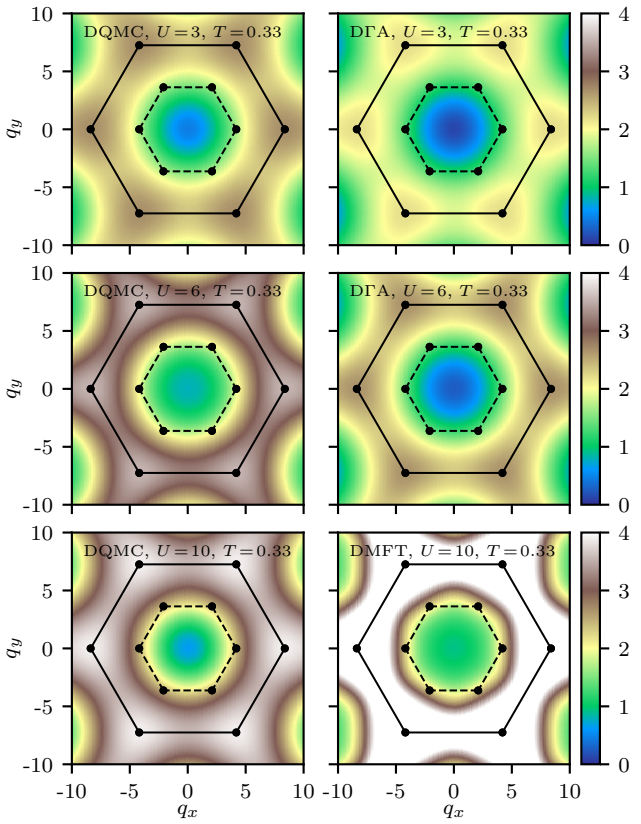

FIG. 10. Equal-time structure factors $S_0(\mathbf{q})$ [Eq. (13)] as a function of U (top to bottom) for DQMC (left), DΓA(top right, middle right), and DMFT (bottom right) at $T = 0.33$. We used the DMFT susceptibility for $U = 10$ to calculate the structure factor, as the respective DΓA calculation did not converge.

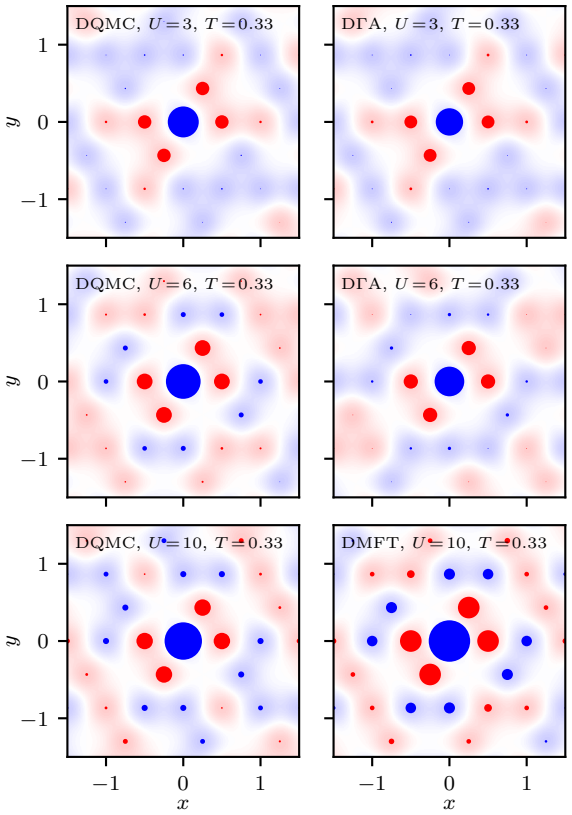

FIG. 11. Equal-time susceptibility $\chi(\mathbf{R} \equiv (x, y))$ as a function of U (top: $U = 6$, bottom: $U = 10$) as calculated by DQMC (left), DΓA(top right) and DMFT (bottom right) at $T = 0.33$. The area of a circle reflects the absolute value of the respective term, blue color denotes positive (ferromagnetic) correlations, red color denotes negative (antiferromagnetic) correlations. Note that weak long-range correlations are ferromagnetic for $\mathbf{R}_2$, $\mathbf{R}_{3a}$ and antiferromagnetic for $\mathbf{R}_{3a}$ (see Table I for the notation of intersite vectors).

at the K-points.

So far, we discussed the structure factor in the weakly correlated regime (U=3). If we now increase the interaction U, we observe an apparent change, both in momentum (Fig. 10) and real (Fig. 11) space. While $S_0(\mathbf{q})$ is still peaked at the K-points, the intensity grows over the entire boundary of the extended Brillouin zone. Again the behavior is understood better by looking at the lattice. Still, antiferromagnetic nearest-neighbor correlations generate the dominating peaks at the K-points, supported by $\mathbf{R}_2$-correlations. However, in the shell of third neighbors now the positive correlations prevail and increase the structure factor at the M-points, i. e. *between* the K-points. This means that the peaks become slightly less separated. More quantitatively, the ratio between the structure factor at the M-point and K-point at $U = 3$ is 0.87 (0.85) in DQMC (DΓA), and it increases to 0.90 (0.87) at $U = 6$.

Interestingly, our patterns are in excellent agreement with the equal-time structure factor computed using numerical linked cluster expansion for the Heisenberg kagome model [125]. We will discuss the ramifications in Sec. IV.

Since our calculations provide direct access to dynamical quantities, it is instructive to inspect the energy dependence of the structure factors. In Fig. 12 we plot the dynamical structure factor $S(\mathbf{q}, \omega)$ on a path through the extended Brillouin zone (Fig. 1) at weak interaction $U = 3$ for two different temperatures. In line with the equal-time structure factor, the dominant weight is located around the K-point. Additionally, there is a splitting into a low- and a high-energy mode at the M-point (cf. Fig. 1, b), although at high energies it is concealed by thermal broadening in DΓA.

Finally, we present the evolution of the dynamical structure factor as a function of correlation strength in Fig. 13. The main effect is squeezing the frequency spread of the intensity to lower energies accompanied by a gradual dissipation of spectral features. Note that it was not possible to converge a self-consistent DΓA calculation for the $U = 10$ case, and in DMFT the spectral

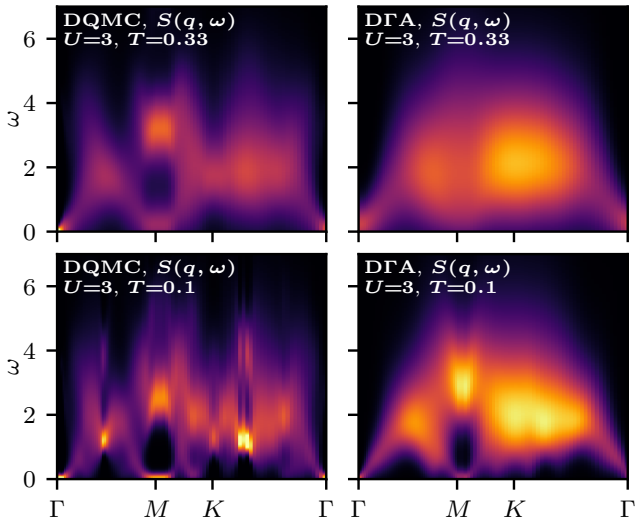

FIG. 12. Dynamical structure factor $S(\mathbf{q},\omega)$ in the weakly correlated regime ($U = 3$) at $T = 0.33$ (top) and $T = 0.1$ (bottom) calculated using DQMC (left) and DΓA (right) on a path through the extended Brillouin zone (Fig. 1).

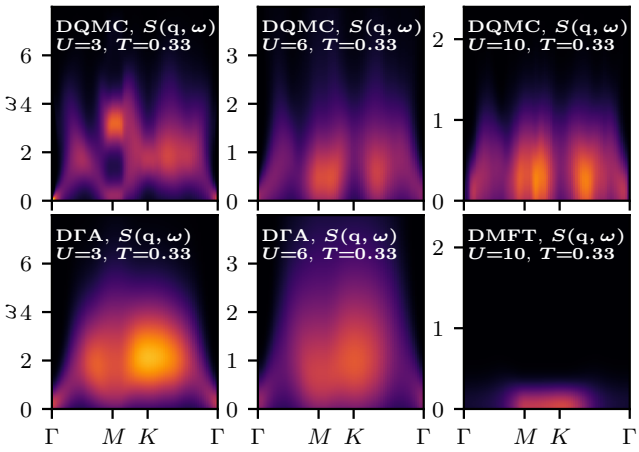

FIG. 13. Dynamical structure factor as a function of interaction strength (left to right) as calculated by DQMC (top) and DΓA(bottom, except for DMFT in the right bottom plot) on a path through the extended Brillouin zone (Fig. 1) at $T = 0.33$. Note that the upper limit of the ω-axis (y-axis) is reduced as $1/U$ upon increasing U to resolve the feature-rich range; for large U such a rescaling must hold as the coupling of the Heisenberg model is $J = 4t^2/U$.

weight is pushed to zero energy.

IV. DISCUSSION

Diagrammatic extensions alleviate the main drawback of DMFT — its restriction to local correlations. An alternative route to include nonlocal correlations are cluster extensions of DMFT. In the conceptually simple cellular DMFT (CMDFT) approach, such clusters are constructed in real space and typically comprise a small number of sites. Correlations in CDMFT are still purely local, but the locality spans now the entire cluster. As a result, nonlocal correlations at the length scale of the cluster are included, while longer-range fluctuations are still absent. In addition to this sharp cutoff between the short-range (included) and long-range (omitted) correlations, CDMFT introduces a spurious disparity between the sites falling within the cluster and all other sites. We can illustrate this by considering the kagome lattice, where each site has four equivalent nearest neighbors. In the simplest possible cluster, a triangle, this equivalence is violated: only two of the four neighboring sites belong to the cluster. Keeping these intrinsic limitations of CDMFT in mind, we compare the results of three different CDMFT studies [66, 129, 130] with our DΓA and DQMC results.

In three-site CDMFT employing a Hirsch-Fye impurity solver, Ohashi *et al.* reported a first-order transition at the critical $U_c = 8.22$ [66]. While we were not aiming at a precise estimate for the critical interaction strength, the three-site CDMFT values is somewhat lower than our DMFT value and higher than our DQMC estimate with 75 sites (and no DMFT bath).

In the strongly correlated regime ($U = 6.6$), the largest eigenvalue of the magnetic susceptibility plotted as a function of $\mathbf{q}$, is nearly flat in CDMFT, with shallow minima along the six Γ-M lines. Precisely this behavior is observed in the DΓA susceptibility (Fig. 6). Interestingly, Ohashi *et al.* report a drastic change of magnetic correlations in the insulating phase: they argue that a starlike structure in the structure factor indicates the onset of 1D antiferromagnetic correlations [66]. We believe that this an artifact of CDMFT. This is corroborated by the fact that the spin correlations that we obtain in DΓA and DQMC for the moderately correlated regime of the Hubbard model are similar to those of the Heisenberg model [125].

The more recent CMDFT study by Udagawa *et al.* [129] employs a continuous-time auxiliary-field QMC impurity solver and uses, in addition to triangles, also more extended nine-site clusters. While the density matrix defined from microscopic states of a cluster is not accessible in the diagrammatic extensions, our temperature-dependent susceptibility (Fig. 7) agrees with the CDMFT results plotted in Fig. 4(d) of Ref. [129], except for the lowest temperatures, where we do not find the downturn of $\chi(T)$ characteristic for antiferromagnetic correlations or the formation of localized dimers. While not much is known for the KHM, we note that in the kagome Heisenberg model, dimer tunneling processes around the loops comprising eight sites play a pivotal role [131]. The absence of such loops in the nine-site clusters used in Ref. [129] may give rise to the formation of static antiferromagnetic dimers, and hence a suppressed susceptibility.

Finally, Kita *et al.* focus on the behavior of the KHM in a magnetic field [130]. Nevertheless, it is instructive to discuss their CDMFT spectral function in zero field, computed for $U = 4$ and $U = 8$ (Fig. 1 in Ref. [130]). The former agrees well with our DΓA results for $U = 3$, except for the substantial broadening in the CDMFT data at low frequencies, which might be an artifact of our analytic continuation. The $U = 8$ case is more interesting. Here, in contrast to single-site DMFT and in agreement with DΓA, no distinct lower Hubbard band is formed; instead, a dispersive feature stemming from the lowest-lying branch of the kagome band structure shows up at low frequencies. Close to the Fermi level, two narrow, nearly dispersionless bands form in CDMFT[130]. We do not observe such structures in our $U = 6$ calculations, neither in DΓA, nor in DQMC: the intensity maxima lie above the Fermi level. At higher frequencies corresponding to the upper Hubbard band, CDMFT shows a broad spectral maximum in the vicinity of the Γ-point which rapidly decreases for finite momenta. A similar, albeit less pronounced distribution of the spectral weight is visible in DΓA results (Fig. 4): the intensity at the Γ-point is maximal.

Structure factors are a direct source of information on the dominant magnetic correlations and instabilities. A prominent example is the antiferromagnetic instability of the square-lattice Hubbard model, signaled by the diverging structure factor at $\mathbf{q} = (\pi, \pi)$, the propagation vector of the Néel state. In contrast, the structure factors of the KHM in the metallic regime lack any apparent instabilities, and instead show an intricate evolution on the frequency/momentum grid. Thus, to get insights into the magnetic correlations, we compare the behavior of $S(\mathbf{q})$ and $S(\mathbf{q}, \omega)$ with the literature data for the Heisenberg model.

The kagome Heisenberg model features several low-lying states with marginally different energies. While the debate on the ground state is still not settled, structure factors recently came into the forefront as a possible fingerprint to distinguish these states experimentally. A popular strategy is to pick a certain candidate state and calculate its structure factor using various mean-field techniques [31, 50, 124, 132–135]. However, in the context of our study, a more appropriate starting point is the direct simulation of the Heisenberg model on a finite lattice, followed by the evaluation of structure factors from the spin correlations. Regardless of the method used, the resulting $S(\mathbf{q})$ of the Heisenberg model smoothly evolves from the minimum at Γ to the maximum at the boundary of the extended Brillouin zone. Further details depend on the computational method: While exact diagonalization on 36-site finite lattices yields feeble, yet discernible peaks at M [136, 137], these features are practically wiped out in density-matrix renormalization group (DMRG) simulations [39, 138] that are less prone to finite-size effects. The featureless structure factor indicates that tendencies to ordering are strongly suppressed, even on a short range. Since they arise from competing correlations, this balance can be destroyed by small deviations from the Heisenberg model, such as anisotropies and/or longer-range exchanges. A common ramification is the appearance of maxima at K or M points of the extended Brillouin zone, indicative of so-called [139] $\sqrt{3}\times\sqrt{3}$ or $\mathbf{q}=0$ antiferromagnetic correlations, respectively.

We are now in the position to compare the equal-time structure factors of the KHM in Figs. 8 and 10 with that of the Heisenberg model. First, the smooth $\mathbf{q}$-evolution and the minimum at Γ are common for both models. For all studied U and T values, the maximal intensity is at K, indicating the predominance of $\sqrt{3}\times\sqrt{3}$ correlations. This is seemingly at odds with the Heisenberg model, where weak maxima, if any, are found at M [136, 137]. However, a key difference lies in the methods: we do calculations at finite temperature. Looking at the finite-temperature structure factors for the Heisenberg model [125], we see a strikingly similar picture: a smooth evolution with maxima at K. This brings us to one of the main conclusions: at moderate temperatures, the magnetic correlations of the KHM are similar to those of the Heisenberg model.

While our equal-time structure factors are quantitatively similar in the weakly and strongly correlated regime (cf. Fig. 8 and Fig. 10), real-space plots of respective susceptibilities reveal a subtle change in third-neighbor correlations (cf. Fig. 9 and Fig. 11). At weak coupling ($U = 3$), Fig. 11 shows along the direction of the two Bravais lattice vectors a negative($\mathbf{R}_1$)-negative($\mathbf{R}_{3a}$)-positive spin correlation function, hinting at tendencies toward a 120° spin-orientation. At strong coupling ($U = 6$ and $U = 10$) the third nearest-neighbor ($\mathbf{R}_{3a}$) changes sign. In the half-filled one-band Hubbard model with a strong negative (antiferromagnetic) preference between nearest neighbors, this is arguably the most dramatic change one might expect, devoid an actual ordering that is prevented by the frustrated lattice. Note that the third nearest neighbors and second nearest neighbors are both at a distance of two hopping elements, they only differ by their distance in real space because of the geometry.

We attribute this difference to the correlation-induced onset of $\mathbf{q} = 0$ magnetic correlations that compete with dominating $\sqrt{3} \times \sqrt{3}$ correlations. At the same time, susceptibilities in the moderately correlated regime (Fig. 11) are qualitatively similar to those in the Heisenberg model [125]. Therefore, we conclude that $\mathbf{q} = 0$ correlations develop already in the moderately correlated regime, i.e. in the metallic phase. This nontrivial result provides a key to distinguish between the weakly and moderately correlated regimes in real materials: The former features predominantly $\sqrt{3}\times\sqrt{3}$ correlations, while in the latter additional $\mathbf{q}=0$ correlations become manifest.

Next, we discuss the features of the dynamical structure factor $S(\mathbf{q}, \omega)$. While details of the plots are prone to uncertainties of the analytic continuation, we comment on one salient feature: the difference between the frequency dependencies at K and M. The highest spectral density is associated with K (consistent with the max-

ima in the equal-time structure factor), but is it shifted to higher frequencies as compared to M. Interestingly, the same structure is found in the structure factor of a Z_2 spin liquid with a moderate spinon-vison interaction [124]. Our work should motivate further studies to clarify whether metallic kagome magnets can serve as a playground for topological vison excitations, which have been suggested in [124].

Finally, we put our results in the context of ongoing experimental activities on metallic kagome magnets. While we computed the quantities that can be measured by inelastic neutron scattering, several aspects impede a direct comparision. First, all so far discovered metallic kagome materials are multi-orbital systems. A simplified effective one-orbital description is generally possible, but the mapping scheme depends on the specifics of a particular material and has to be adjusted accordingly. Second, a kagome-like arrangement of magnetic atoms in the crystal structure does not guarantee the applicability of the KHM: coupling beyond nearest neighbors as well as interplane couplings can play a significant role. This is the case for Mn_3Sn, where neutron scattering experiments reveal the relevance of multiple magnetic exchanges [102]. Bilayer kagome systems Fe_3Sn_2 [88] and $Co_3Sn_2S_2$ [98] that entail a sizable interlayer coupling fall in the same category. Also the band filling, whose estimation in a real material is per se challenging, can deviate from the case in point: KHM at strict half-filling. All in all, we believe that presently the most promising case is FeSn, whose band structure (Fig. 4 in Ref. [102]) bears apparent similarities to the half-filled tight-binding kagome model. We are looking forward to future inelastic neutron scattering experiments (announced in Ref. [104]) that can be compared with our structure factors and dynamical susceptibilities.

V. CONCLUSION

We studied the phase diagram and the magnetic structure factor of the kagome Hubbard model, focusing on the weakly and moderately correlated regime relevant for the growing family of real materials. To this end, we employed three complementary methods: DMFT, DΓA and DQMC. We observe neither tendencies towards magnetic ordering of any kind, nor fingerprints of singlet formation. To provide solid reference data for inelastic neutron scattering experiments on candidate materials, we calculate dynamical as well as equal-time structure factors and susceptibilities, for a wide range of the interaction parameters U and at different temperatures. By comparing our results with the literature data for the Heisenberg model, we conclude that the Mott transition is not accompanied by a sensible alteration of magnetic correlations: the major change happens already in the metallic phase, where the magnetic coupling to third-nearest neighbors changes sign. We argue that this change gives a key to estimate U, and hence the proximity to a metal-to-insulator transition, in real materials.

ACKNOWLEDGMENTS

We are grateful to Daniel Hirschmeier and Alexander Lichtenstein for inspiring discussions and their help in the early stages of this project; furthermore, we thank them and Andrey Lehmann for sharing preliminary results of their dual fermion calculations. We acknowledge fruitful discussions with Evgeny Stepanov, Joseph Checkelsky, Linda Ye, Shiang Fang, Satoshi Nishimoto, and Johannes Richter. J. K. further thanks Malte Rösner, Clio Agrapidis and Lukas Rammelmüller for useful comments. Calculations have been done on the Vienna Scientific Cluster (VSC) and the computational facilities of the Leibniz IFW Dresden. We thank U. Nitzsche for technical assistance. Plots were made using the matplotlib [140] plotting library for python. J. K. and K. S. thank the Leibniz IFW Dresden and UC Davis, respectively, for hospitality during their stay. O. J. was supported by the Leibniz Association through the Leibniz Competition; J. K. and K. H. by the Austrian science fund (FWF) through projects P 32044 and P 30997; K. S. by the Marshall Plan Scholarships Program; the work of R. T. S. was supported by the grant DE–SC0014671 funded by the U.S. Department of Energy, Office of Science.

Appendix: Fingerprint of real-space correlations

For a better understanding of how spin-spin correlations between certain points in the lattice affect the susceptibility or structure factor in momentum space, it is helpful to study the connection analytically. The basis for this is Eq. (11), where we set $\langle S_z^j(\mathbf{R},\tau)S_z^l(\mathbf{0},0)\rangle = 1$ for a certain vector $\mathbf{R}$ and all vectors that are related by symmetry transformations. Fig. 14 shows, row by row, how correlations to a certain neighbor $\mathbf{R}$ and its symmetrically related counterparts reflect in $\mathbf{k}$-space. The first three rows are the projections to tight-binding eigenstates, and the fourth row is the structure factor.

Unsurprisingly, on-site correlations yield just a constant contribution. $\mathbf{R}_1$- and $\mathbf{R}_2$-correlations lead to peaks at the K-point in the extended Brillouin zone, whereas $\mathbf{R}_3$-correlations enhance the M-point (last two rows in Fig. 14).

It is important to note that, for this analysis, we always consider positive correlations (of unit magnitude) between neighboring sites at the indicated distance, negative ones just change the sign. For the nearest-neighbor correlations ($\mathbf{R}_1$) this means, e.g., that we get negative peaks at the K-points, whereas the actual correlations at $\mathbf{R}_1$ are negative yielding positiv peaks around the K-points. Furthermore let us note that the number of neighbors at $\mathbf{R}_{3a}$ is twice as large as the number of neighbors at $\mathbf{R}_{3b}$. Therefore also their influence on the structure factor is twice as large.

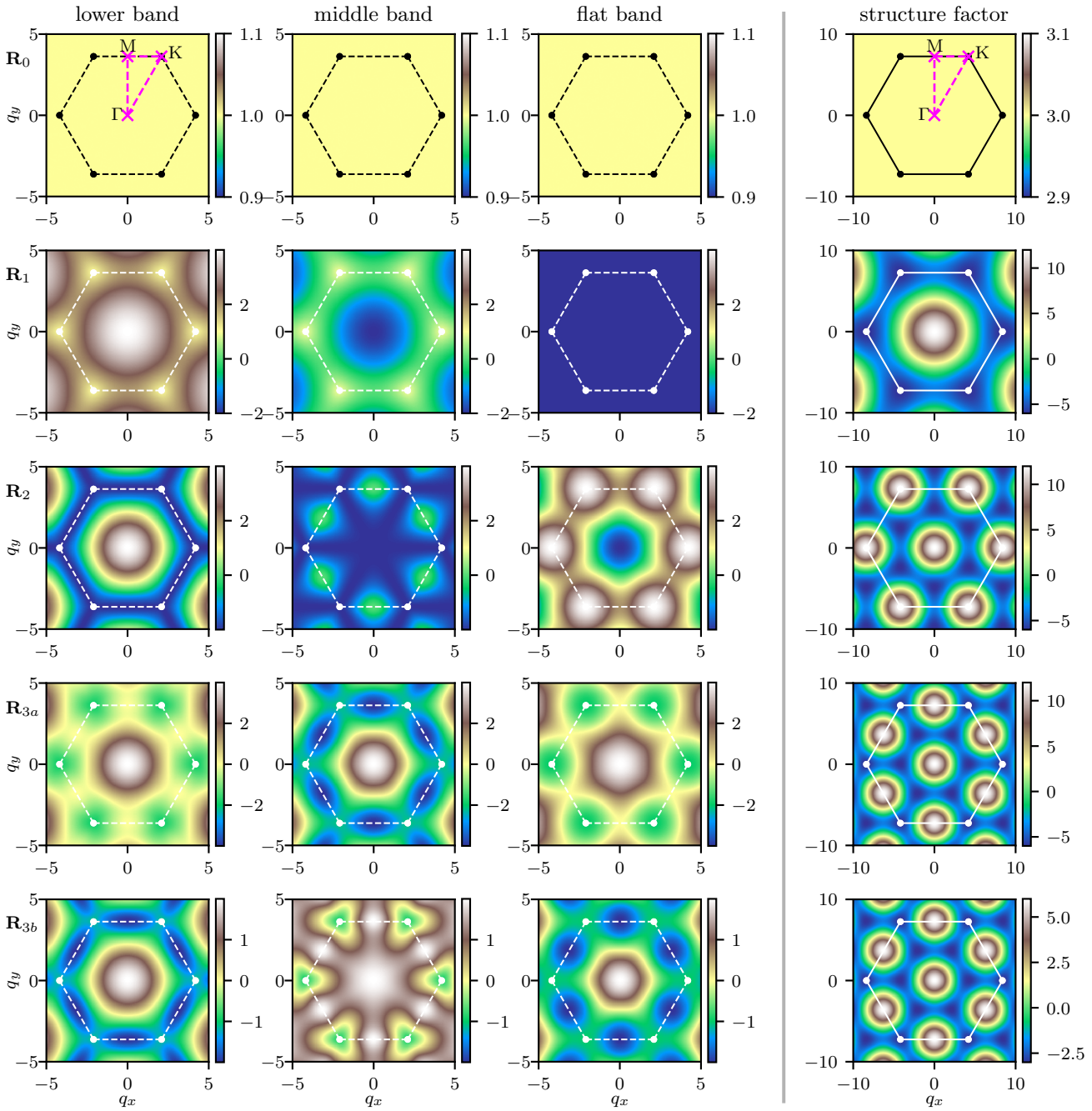

FIG. 14. How certain real-space correlations influence the magnetic susceptibility and structure factor. In the first three columns we show the projection of the magnetic susceptibility on the lower-band, middle-band and flat-band eigenstates of the tight-binding Hamiltonian, respectively. The right-most column shows the corresponding structure factor $S(\mathbf{q})$ on the extended Brillouin zone. The rows correspond to various correlations in real space: Thus in the first row we show momentum-space correlations arising from on-site correlations. The second row corresponds to nearest-neighbor correlations ($\mathbf{R}_1$). The third, fourth and fifth row correspond to $\mathbf{R}_2$, $\mathbf{R}_{3a}$ and $\mathbf{R}_{3b}$ correlations.

[1] E. Dagotto, *Complexity in Strongly Correlated Electronic Systems*, Science **309**, 257 (2005).

[2] D. Pesin and L. Balents, *Mott physics and band topology in materials with strong spin-orbit interaction*, Nature Phys. **6**, 376 (2010).

[3] D. N. Basov, R. D. Averitt, D. van der Marel, M. Dressel, and K. Haule, *Electrodynamics of correlated electron materials*, Rev. Mod. Phys. **83**, 471 (2011).

[4] M. Imada and T. Miyake, *Electronic Structure Calculation by First Principles for Strongly Correlated Electron Systems*, J. Phys. Soc. Jpn. **79**, 112001 (2010).

[5] J. Kanamori, *Electron Correlation and Ferromagnetism of Transition Metals*, Progr. Theor. Phys. **30**, 275 (1963).

[6] J. Hubbard, *Electron Correlations in Narrow Energy Bands*, Proc. Royal Soc. London. Series A, Mat. Phys. Sci. **276**, 238 (1963).

[7] M. C. Gutzwiller, *Effect of Correlation on the Ferromagnetism of Transition Metals*, Phys. Rev. Lett. **10**, 159 (1963).

[8] M. Imada, A. Fujimori, and Y. Tokura, *Metal-insulator transitions*, Rev. Mod. Phys. **70**, 1039 (1998).

[9] P. W. Anderson, *Localized Magnetic States in Metals*, Phys. Rev. **124**, 41 (1961).

[10] W. E. Pickett, *Electronic structure of the high-temperature oxide superconductors*, Rev. Mod. Phys. **61**, 433 (1989).

[11] E. H. Lieb and F. Y. Wu, *Absence of Mott Transition in an Exact Solution of the Short-Range, One-Band Model in One Dimension*, Phys. Rev. Lett. **20**, 1445 (1968).

[12] A. Georges and G. Kotliar, *Hubbard model in infinite dimensions*, Phys. Rev. B **45**, 6479 (1992).

[13] A. Georges, G. Kotliar, W. Krauth, and M. J. Rozenberg, *Dynamical mean-field theory of strongly correlated fermion systems and the limit of infinite dimensions*, Rev. Mod. Phys. **68**, 13 (1996).

[14] W. Metzner and D. Vollhardt, *Correlated Lattice Fermions in d=∞ Dimensions*, Phys. Rev. Lett. **62**, 324 (1989).

[15] E. Müller-Hartmann, *Correlated fermions on a lattice in high dimensions*, Z. Phys. B **74**, 507 (1989).

[16] M. Jarrell, *Hubbard model in infinite dimensions: A quantum Monte Carlo study*, Phys. Rev. Lett. **69**, 168 (1992).

[17] B. Keimer, S. A. Kivelson, M. R. Norman, S. Uchida, and J. Zaanen, *From quantum matter to high-temperature superconductivity in copper oxides*, Nature (London) **518**, 179 (2015).

[18] Y. Cao, V. Fatemi, A. Demir, S. Fang, S. L. Tomarken, J. Y. Luo, J. D. Sanchez-Yamagishi, K. Watanabe, T. Taniguchi, E. Kaxiras, R. C. Ashoori, and P. Jarillo-Herrero, *Correlated insulator behaviour at half-filling in magic-angle graphene superlattices*, Nature (London) **556**, 80 (2018).

[19] J. Mannhart and D. G. Schlom, *Oxide Interfaces — An Opportunity for Electronics*, Science **327**, 1607 (2010).

[20] H. Y. Hwang, Y. Iwasa, M. Kawasaki, B. Keimer, N. Nagaosa, and Y. Tokura, *Emergent phenomena at oxide interfaces*, Nature Mater. **11**, 103 (2012).

[21] T. Schäfer, F. Geles, D. Rost, G. Rohringer, E. Arrigoni, K. Held, N. Blümer, M. Aichhorn, and A. Toschi, *Fate of the false Mott-Hubbard transition in two dimensions*, Phys. Rev. B **91**, 125109 (2015).

[22] T. Schäfer, N. Wentzell, F. Šimkovic IV, Y.-Y. He, C. Hille, M. Klett, C. J. Eckhardt, B. Arzhang, V. Harkov, F.-M. L. Régent, A. Kirsch, Y. Wang, A. J. Kim, E. Kozik, E. A. Stepanov, A. Kauch, S. Andergassen, P. Hansmann, D. Rohe, Y. M. Vilk, J. P. F. LeBlanc, S. Zhang, A. M. S. Tremblay, M. Ferrero, O. Parcollet, and A. Georges, *Tracking the Footprints of Spin Fluctuations: A Multi-Method, Multi-Messenger Study of the Two-Dimensional Hubbard Model* (2020), arXiv:2006.10769 [cond-mat.str-el].

[23] S. R. White, D. J. Scalapino, R. L. Sugar, E. Y. Loh, J. E. Gubernatis, and R. T. Scalettar, *Numerical study of the two-dimensional Hubbard model*, Phys. Rev. B **40**, 506 (1989).

[24] J. E. Hirsch and S. Tang, *Antiferromagnetism in the Two-Dimensional Hubbard Model*, Phys. Rev. Lett. **62**, 591 (1989).

[25] C. N. Varney, C.-R. Lee, Z. J. Bai, S. Chiesa, M. Jarrell, and R. T. Scalettar, *Quantum Monte Carlo study of the two-dimensional fermion Hubbard model*, Phys. Rev. B **80**, 075116 (2009).

[26] A. E. Antipov, A. N. Rubtsov, M. I. Katsnelson, and A. I. Lichtenstein, *Electron energy spectrum of the spin-liquid state in a frustrated Hubbard model*, Phys. Rev. B **83**, 115126 (2011).

[27] G. Li, A. E. Antipov, A. N. Rubtsov, S. Kirchner, and W. Hanke, *Competing phases of the Hubbard model on a triangular lattice: Insights from the entropy*, Phys. Rev. B **89**, 161118 (2014).

[28] Y. Ran, M. Hermele, P. A. Lee, and X.-G. Wen, *Projected-Wave-Function Study of the spin-1/2 Heisenberg Model on the Kagome Lattice*, Phys. Rev. Lett. **98**, 117205 (2007).

[29] M. Hermele, Y. Ran, P. A. Lee, and X.-G. Wen, *Properties of an algebraic spin liquid on the kagome lattice*, Phys. Rev. B **77**, 224413 (2008).

[30] O. Ma and J. B. Marston, *Weak Ferromagnetic Exchange and Anomalous Specific Heat in $ZnCu_3OH_6Cl_2$*, Phys. Rev. Lett. **101**, 027204 (2008).

[31] Y. Iqbal, F. Becca, S. Sorella, and D. Poilblanc, *Gapless spin-liquid phase in the kagome spin-$\frac{1}{2}$ Heisenberg antiferromagnet*, Phys. Rev. B **87**, 060405 (2013).

[32] Y.-C. He, M. P. Zaletel, M. Oshikawa, and F. Pollmann, *Signatures of Dirac cones in a DMRG study of the Kagome Heisenberg model*, Phys. Rev. X **7**, 031020 (2017).

[33] H. J. Liao, Z. Y. Xie, J. Chen, Z. Y. Liu, H. D. Xie, R. Z. Huang, B. Normand, and T. Xiang, *Gapless Spin-Liquid Ground State in the $S = 1/2$ Kagome Antiferromagnet*, Phys. Rev. Lett. **118**, 137202 (2017).

[34] X. Chen, S.-J. Ran, T. Liu, C. Peng, Y.-Z. Huang, and G. Su, *Thermodynamics of spin-1/2 Kagomé Heisenberg antiferromagnet: algebraic paramagnetic liquid and finite-temperature phase diagram*, Sci. Bull. **63**, 1545 (2018).

[35] S. Yan, D. A. Huse, and S. R. White, *Spin Liquid Ground State of the S=1/2 Kagome Heisenberg Antiferromagnet*, Science **332**, 1173 (2011).

[36] S. Depenbrock, I. P. McCulloch, and U. Schollwöck, *Na-*

ture of the Spin-Liquid Ground State of the $S = 1/2$ Heisenberg Model on the Kagome Lattice, Phys. Rev. Lett. **109**, 067201 (2012).

[37] H.-C. Jiang, Z. Wang, and L. Balents, *Identifying topological order by entanglement entropy*, Nat. Phys. **8**, 902 (2012).

[38] S. Nishimoto, N. Shibata, and C. Hotta, *Controlling frustrated liquids and solids with an applied field in a kagome Heisenberg antiferromagnet*, Nat. Commun. **4**, 2287 (2013).

[39] F. Kolley, S. Depenbrock, I. P. McCulloch, U. Schollwöck, and V. Alba, *Phase diagram of the J_1-J_2 Heisenberg model on the kagome lattice*, Phys. Rev. B **91**, 104418 (2015).

[40] J.-W. Mei, J.-Y. Chen, H. He, and X.-G. Wen, *Gapped spin liquid with $\mathbb{Z}_2$ topological order for the kagome Heisenberg model*, Phys. Rev. B **95**, 235107 (2017).

[41] A. M. Läuchli, J. Sudan, and R. Moessner, *$S = \frac{1}{2}$ kagome Heisenberg antiferromagnet revisited*, Phys. Rev. B **100**, 155142 (2019).

[42] L. Messio, B. Bernu, and C. Lhuillier, *Kagome Antiferromagnet: A Chiral Topological Spin Liquid?*, Phys. Rev. Lett. **108**, 207204 (2012).

[43] S. Capponi, V. R. Chandra, A. Auerbach, and M. Weinstein, *p6 chiral resonating valence bonds in the kagome antiferromagnet*, Phys. Rev. B **87**, 161118 (2013).

[44] S.-S. Gong, W. Zhu, and D. N. Sheng, *Emergent Chiral Spin Liquid: Fractional Quantum Hall Effect in a Kagome Heisenberg Model*, Sci. Rep. **4**, 6713 (2014).

[45] B. Bauer, L. Cincio, B. P. Keller, M. Dolfi, G. Vidal, S. Trebst, and A. Ludwig, *Chiral spin liquid and emergent anyons in a Kagome lattice Mott insulator*, Nat. Commun. **5**, 5137 (2014).

[46] Y.-C. He, D. N. Sheng, and Y. Chen, *Chiral Spin Liquid in a Frustrated Anisotropic Kagome Heisenberg Model*, Phys. Rev. Lett. **112**, 137202 (2014).

[47] A. Wietek, A. Sterdyniak, and A. M. Läuchli, *Nature of chiral spin liquids on the kagome lattice*, Phys. Rev. B **92**, 125122 (2015).

[48] S.-S. Gong, W. Zhu, L. Balents, and D. N. Sheng, *Global phase diagram of competing ordered and quantum spin-liquid phases on the kagome lattice*, Phys. Rev. B **91**, 075112 (2015).

[49] W.-J. Hu, W. Zhu, Y. Zhang, S. Gong, F. Becca, and D. N. Sheng, *Variational Monte Carlo study of a chiral spin liquid in the extended Heisenberg model on the kagome lattice*, Phys. Rev. B **91**, 041124 (2015).

[50] L. Messio, S. Bieri, C. Lhuillier, and B. Bernu, *Chiral Spin Liquid on a Kagome Antiferromagnet Induced by the Dzyaloshinskii-Moriya Interaction*, Phys. Rev. Lett. **118**, 267201 (2017).

[51] J. B. Marston and C. Zeng, *Spin-Peierls and spin-liquid phases of Kagome quantum antiferromagnets*, J. Appl. Phys. **69**, 5962 (1991).

[52] A. V. Syromyatnikov and S. V. Maleyev, *Hidden long-range order in kagomé Heisenberg antiferromagnets*, Phys. Rev. B **66**, 132408 (2002).

[53] P. Nikolic and T. Senthil, *Physics of low-energy singlet states of the Kagome lattice quantum Heisenberg antiferromagnet*, Phys. Rev. B **68**, 214415 (2003).

[54] R. R. P. Singh and D. A. Huse, *Ground state of the spin-1/2 kagome-lattice Heisenberg antiferromagnet*, Phys. Rev. B **76**, 180407 (2007).

[55] R. Budnik and A. Auerbach, *Low-Energy Singlets in the Heisenberg Antiferromagnet on the Kagome Lattice*, Phys. Rev. Lett. **93**, 187205 (2004).

[56] G. Evenbly and G. Vidal, *Frustrated Antiferromagnets with Entanglement Renormalization: ground State of the Spin-1/2 Heisenberg Model on a Kagome Lattice*, Phys. Rev. Lett. **104**, 187203 (2010).

[57] D. Schwandt, M. Mambrini, and D. Poilblanc, *Generalized hard-core dimer model approach to low-energy Heisenberg frustrated antiferromagnets: general properties and application to the kagome antiferromagnet*, Phys. Rev. B **81**, 214413 (2010).

[58] D. Poilblanc, M. Mambrini, and D. Schwandt, *Effective quantum dimer model for the kagome Heisenberg antiferromagnet: nearby quantum critical point and hidden degeneracy*, Phys. Rev. B **81**, 180402 (2010).

[59] D. Poilblanc and G. Misguich, *Competing valence bond crystals in the kagome quantum dimer model*, Phys. Rev. B **84**, 214401 (2011).

[60] J. S. Helton, K. Matan, M. P. Shores, E. A. Nytko, B. M. Bartlett, Y. Yoshida, Y. Takano, A. Suslov, Y. Qiu, J.-H. Chung, D. G. Nocera, and Y. S. Lee, *Spin Dynamics of the Spin-1/2 Kagome Lattice Antiferromagnet $ZnCu_3(OH)_6Cl_2$*, Phys. Rev. Lett. **98**, 107204 (2007).

[61] T.-H. Han, J. S. Helton, S. Chu, D. G. Nocera, J. A. Rodriguez-Rivera, C. Broholm, and Y. S. Lee, *Fractionalized excitations in the spin-liquid state of a kagome-lattice antiferromagnet*, Nature **492**, 406 (2012).

[62] P. Khuntia, M. Velazquez, Q. Barthélemy, F. Bert, E. Kermarrec, A. Legros, B. Bernu, L. Messio, A. Zorko, and P. Mendels, *Gapless ground state in the archetypal quantum kagome antiferromagnet $ZnCu_3(OH)_6Cl_2$*, Nat. Phys. **16**, 469 (2020).

[63] P. Mendels, F. Bert, M. A. de Vries, A. Olariu, A. Harrison, F. Duc, J. C. Trombe, J. S. Lord, A. Amato, and C. Baines, *Quantum Magnetism in the Paratacamite Family: towards an Ideal Kagome Lattice*, Phys. Rev. Lett. **98**, 077204 (2007).

[64] O. Janson, *DFT-based microscopic magnetic modeling for low-dimensional spin systems*, Ph.D. thesis, Technische Universität Dresden (2012).

[65] H. O. Jeschke, F. Salvat-Pujol, and R. Valentí, *First-principles determination of Heisenberg Hamiltonian parameters for the spin-$\frac{1}{2}$ kagome antiferromagnet $ZnCu_3(OH)_6Cl_2$*, Phys. Rev. B **88**, 075106 (2013).

[66] T. Ohashi, N. Kawakami, and H. Tsunetsugu, *Mott Transition in Kagomé Lattice Hubbard Model*, Phys. Rev. Lett. **97**, 066401 (2006).

[67] T. Ohashi, S. Suga, N. Kawakami, and H. Tsunetsugu, *Magnetic correlations around the Mott transition in the Kagomé lattice Hubbard model*, J. Phys.: Condens. Matter **19**, 145251 (2007).

[68] R. Higa and K. Asano, *Bond formation effects on the metal-insulator transition in the half-filled kagome Hubbard model*, Phys. Rev. B **93**, 245123 (2016).

[69] K. Kudo, T. Yoshida, and Y. Hatsugai, *Higher-order Topological Mott Insulators*, Phys. Rev. Lett. **123**, 196402 (2019).

[70] I. I. Mazin, H. O. Jeschke, F. Lechermann, H. Lee, M. Fink, R. Thomale, and R. Valenti, *Theoretical prediction of a strongly correlated Dirac metal*, Nat. Commun. **5**, 4261 (2014).

[71] O. Janson, J. Richter, and H. Rosner, *Modified Kagome Physics in the Natural Spin-1/2 Kagome Lattice Systems: kapellasite $Cu_3Zn(OH)_6Cl_2$ and haydeeite*

$Cu_3Mg(OH)_6Cl_2$, Phys. Rev. Lett. **101**, 106403 (2008).
[72] B. Fåk, E. Kermarrec, L. Messio, B. Bernu, C. Lhuillier, F. Bert, P. Mendels, B. Koteswararao, F. Bouquet, J. Ollivier, A. D. Hillier, A. Amato, R. H. Colman, and A. S. Wills, *Kapellasite: A Kagome Quantum Spin Liquid with Competing Interactions*, Phys. Rev. Lett. **109**, 037208 (2012).
[73] Y. Iqbal, H. O. Jeschke, J. Reuther, R. Valentí, I. I. Mazin, M. Greiter, and R. Thomale, *Paramagnetism in the kagome compounds (Zn,Mg,Cd)$Cu_3(OH_6)Cl_2$*, Phys. Rev. B **92**, 220404 (2015).
[74] S. Nakatsuji, N. Kiyohara, and T. Higo, *Large anomalous Hall effect in a non-collinear antiferromagnet at room temperature*, Nature (London) **527**, 212 (2015).
[75] A. K. Nayak, J. E. Fischer, Y. Sun, B. Yan, J. Karel, A. C. Komarek, C. Shekhar, N. Kumar, W. Schnelle, J. Kübler, C. Felser, and S. S. P. Parkin, *Large anomalous Hall effect driven by a nonvanishing Berry curvature in the noncolinear antiferromagnet Mn_3Ge*, Sci. Adv. **2**, e1501870 (2016).
[76] K. Kuroda, T. Tomita, M.-T. Suzuki, C. Bareille, A. A. Nugroho, P. Goswami, M. Ochi, M. Ikhlas, M. Nakayama, S. Akebi, R. Noguchi, R. Ishii, N. Inami, K. Ono, H. Kumigashira, A. Varykhalov, T. Muro, T. Koretsune, R. Arita, S. Shin, T. Kondo, and S. Nakatsuji, *Evidence for magnetic Weyl fermions in a correlated metal*, Nat. Mater. **16**, 1090 (2017).
[77] M. Kimata, H. Chen, K. Kondou, S. Sugimoto, P. K. Muduli, M. Ikhlas, Y. Omori, T. Tomita, A. H. MacDonald, S. Nakatsuji, and Y. Otani, *Magnetic and magnetic inverse spin Hall effects in a non-collinear antiferromagnet*, Nature **565**, 627 (2019).
[78] X. Li, C. Collignon, L. Xu, H. Zuo, A. Cavanna, U. G. D. Mailly, B. Fauqué, L. Balents, Z. Zhu, and K. Behnia, *Chiral domain walls of Mn_3Sn and their memory*, Nat. Commun. **10**, 3021 (2019).
[79] C. Wuttke, F. Caglieris, S. Sykora, F. Scaravaggi, A. U. B. Wolter, K. Manna, V. Süss, C. Shekhar, C. Felser, B. Büchner, and C. Hess, *Berry curvature unravelled by the anomalous Nernst effect in Mn_3Ge*, Phys. Rev. B **100**, 085111 (2019).
[80] L. A. Fenner, A. A. Dee, and A. S. Wills, *Non-collinearity and spin frustration in the itinerant kagome ferromagnet Fe_3Sn_2*, J. Phys.: Condens. Matter **21**, 452202 (2009).
[81] T. Kida, L. A. Fenner, A. A. Dee, I. Terasaki, M. Hagiwara, and A. S. Wills, *The giant anomalous Hall effect in theferromagnet Fe_3Sn_2 — a frustrated kagome metal*, J. Phys.: Condens. Matter **23**, 112205 (2011).
[82] Z. Hou, W. Ren, B. Ding, G. Xu, Y. Wang, B. Yang, Q. Zhang, Y. Zhang, E. Liu, F. Xu, W. Wang, G. Wu, X. Zhang, B. Shen, and Z. Zhang, *Observation of Various and Spontaneous Magnetic Skyrmionic Bubbles at Room Temperature in a Frustrated Kagome Magnet with Uniaxial Magnetic Anisotropy*, Adv. Mater. **29**, 1701144 (2017).
[83] L. Ye, M. Kang, J. Liu, F. von Cube, C. R. Wicker, T. Suzuki, C. Jozwiak, A. Bostwick, E. Rotenberg, David, Bell, L. Fu, R. Comin, and J. G. Checkelsky, *Massive Dirac fermions in a ferromagnetic kagome metal*, Nature **555**, 638 (2018).
[84] J.-X. Yin, S. S. Zhang, H. Li, K. Jiang, G. Chang, B. Zhang, B. Lian, C. Xiang, I. Belopolski, H. Zheng, T. A. Cochran, S.-Y. Xu, G. Bian, K. Liu, T.-R. Chang, H. Lin, Z.-Y. Lu, Z. Wang, S. Jia, W. Wang, and M. Z. Hasan, *Giant and anisotropic many-body spin-orbit tunability in a strongly correlated kagome magnet*, Nature **562**, 91 (2018).
[85] Z. Lin, J.-H. Choi, Q. Zhang, W. Qin, S. Yi, P. Wang, L. Li, Y. Wang, H. Zhang, Z. Sun, L. Wei, S. Zhang, T. Guo, Q. Lu, J.-H. Cho, C. Zeng, and Z. Zhang, *Flatbands and Emergent Ferromagnetic Ordering in Fe_3Sn_2 Kagome Lattices*, Phys. Rev. Lett. **121**, 096401 (2018).
[86] H. Li, B. Ding, J. Chen, Z. Li, Z. Hou, E. Liu, H. Zhang, X. Xi, G. Wu, and W. Wang, *Large topological Hall effect in a geometrically frustrated kagome magnet Fe_3Sn_2*, Appl. Phys. Lett. **114**, 192408 (2019).
[87] Y. Li, Q. Wang, L. DeBeer-Schmitt, Z. Guguchia, R. D. Desautels, J.-X. Yin, Q. Du, W. Ren, X. Zhao, Z. Zhang, I. A. Zaliznyak, C. Petrovic, W. Yin, M. Z. Hasan, H. Lei, and J. M. Tranquada, *Magnetic-Field Control of Topological Electronic Response near Room Temperature in Correlated Kagome Magnets*, Phys. Rev. Lett. **123**, 196604 (2019).
[88] H. Tanaka, Y. Fujisawa, K. Kuroda, R. Noguchi, S. Sakuragi, C. Bareille, B. Smith, C. Cacho, S. W. Jung, T. Muro, Y. Okada, and T. Kondo, *Three-dimensional electronic structure in ferromagnetic Fe_3Sn_2 with breathing kagome bilayers*, Phys. Rev. B **101**, 161114 (2020).
[89] E. Liu, Y. Sun, N. Kumar, L. Muechler, A. Sun, L. Jiao, S.-Y. Yang, D. Liu, A. Liang, Q. Xu, J. Kroder, V. Süß, H. Borrmann, C. Shekhar, Z. Wang, C. Xi, W. Wang, W. Schnelle, S. Wirth, Y. Chen, S. T. B. Goennenwein, and C. Felser, *Giant anomalous Hall effect in a ferromagnetic kagome-lattice semimetal*, Nat. Phys. **14**, 1125 (2018).
[90] Q. Wang, Y. Xu, R. Lou, Z. Liu, M. Li, Y. Huang, H. Weng, S. Wang, and H. Lei, *Large intrinsic anomalous Hall effect in half-metallic ferromagnet $Co_3Sn_2S_2$ with magnetic Weyl fermions*, Nat. Commun. **9**, 3681 (2018).
[91] J.-X. Yin, S. S. Zhang, G. Chang, Q. Wang, S. S. Tsirkin, Z. Guguchia, B. Lian, H. Zhou, K. Jiang, I. Belopolski, N. Shumiya, D. Multer, M. Litskevich, T. A. Cochran, H. Lin, Z. Wang, T. Neupert, S. Jia, H. Lei, and M. Z. Hasan, *Negative flat band magnetism in a spin-orbit-coupled correlated kagome magnet*, Nat. Phys. **15**, 443 (2019).
[92] D. F. Liu, A. J. Liang, E. K. Liu, Q. N. Xu, Y. W. Li, C. Chen, D. Pei, W. J. Shi, S. K. Mo, P. Dudin, T. Kim, C. Cacho, G. Li, Y. Sun, L. X. Yang, Z. K. Liu, S. S. P. Parkin, C. Felser, , and Y. L. Chen, *Magnetic Weyl semimetal phase in a Kagomé crystal*, Science **365**, 1282 (2019).
[93] J. Shen, Q. Zeng, S. Zhang, W. Tong, L. Ling, C. Xi, Z. Wang, E. Liu, W. Wang, G. Wu, and B. Shen, *On the anisotropies of magnetization and electronic transport of magnetic Weyl semimetal $Co_3Sn_2S_2$*, Appl. Phys. Lett. **115**, 212403 (2019).
[94] E. Lachman, R. A. Murphy, N. Maksimovic, R. Kealhofer, S. Haley, R. D. McDonald, J. R. Long, and J. G. Analytis, *Exchange biased anomalous Hall effect driven by frustration in a magnetic kagome lattice*, Nat. Commun. **11**, 560 (2020).
[95] S. Howard, L. Jiao, Z. Wang, P. Vir, C. Shekhar, C. Felser, T. Hughes, and V. Madhavan, *Observation of linearly dispersive edge modes in a magnetic Weyl*

semimetal $Co_3Sn_2S_2$ (2019), arXiv:1910.11205 [cond-mat.mtrl-sci].

[96] Y. Xing, J. Shen, H. Chen, Y. Gao, Y.-Y. Zhang, G. Li, B. Hu, G. Qian, X. Zhang, P. Fan, Q. Wang, Q. Yin, H. Lei, W. Ji, S. Du, H. Yang, C. Shen, E. Liu, B. Shen, Z. Wang, and H.-J. Gao, *Localized spin-orbit polaron in magnetic Weyl semimetal $Co_3Sn_2S_2$* (2020), arXiv:2001.11295 [cond-mat.mtrl-sci].

[97] J.-X. Yin, N. Shumiya, Y. Jiang, H. Zhou, G. Macam, H. O. M. Sura, S. S. Zhang, Z.-J. Cheng, Z. Guguchia, Y. Li, Q. Wang, M. Litskevich, I. Belopolski, X. P. Yang, T. A. Cochran, G. Chang, Q. Zhang, Z.-Q. Huang, F.-C. Chuang, H. Lin, H. Lei, B. M. Andersen, Z. Wang, S. Jia, and M. Z. Hasan, *Spin-orbit quantum impurity in a topological magnet*, Nat. Commun. **11**, 4415 (2020).

[98] C. Liu, J. Shen, J. Gao, C. Yi, D. Liu, T. Xie, L. Yang, S. Danilkin, G. Deng, W. Wang, S. Li, Y. Shi, H. Weng, E. Liu, and H. Luo, *Spin excitations and spin wave gap in the ferromagnetic Weyl semimetal $Co_3Sn_2S_2$*, China Phys. Mech. Astron. **64**, 217062 (2021).

[99] S. Nakamura, N. Kabeya, M. Kobayashi, K. Araki, K. Katoh, and A. Ochiai, *Spin trimer formation in the metallic compound $Gd_3Ru_4Al_{12}$ with a distorted kagome lattice structure*, Phys. Rev. B **98**, 054410 (2018).

[100] T. Matsumura, Y. Ozono, S. Nakamura, N. Kabeya, and A. Ochiai, *Helical Ordering of Spin Trimers in a Distorted Kagome Lattice of $Gd_3Ru_4Al_{12}$ Studied by Resonant X-ray Diffraction*, J. Phys. Soc. Jpn. **88**, 023704 (2019).

[101] H. Inoue, M. Han, L. Ye, T. Suzuki, and J. G. Checkelsky, *Molecular beam epitaxy growth of antiferromagnetic Kagome metal FeSn*, Appl. Phys. Lett **115**, 072403 (2019).

[102] M. Kang, L. Ye, S. Fang, J.-S. You, A. Levitan, M. Han, J. I. Facio, C. Jozwiak, A. Bostwick, E. Rotenberg, M. K. Chan, R. D. McDonald, D. Graf, K. Kaznatcheev, E. Vescovo, D. C. Bell, E. Kaxiras, J. van den Brink, M. Richter, M. P. Ghimire, J. G. Checkelsky, and R. Comin, *Dirac fermions and flat bands in the ideal kagome metal FeSn*, Nat. Mater. **19**, 163 (2019).

[103] Z. Lin, C. Wang, P. Wang, S. Yi, L. Li, Q. Zhang, Y. Wang, Z. Wang, H. Huang, Y. Sun, Y. Huang, D. Shen, D. Feng, Z. Sun, J.-H. Cho, C. Zeng, and Z. Zhang, *Dirac fermions in antiferromagnetic FeSn kagome lattices with combined space inversion and time-reversal symmetry*, Phys. Rev. B **102**, 155103 (2020).

[104] B. C. Sales, J. Yan, W. R. Meier, A. D. Christianson, S. Okamoto, and M. A. McGuire, *Electronic, magnetic, and thermodynamic properties of the kagome layer compound FeSn*, Phys. Rev. Materials **3**, 114203 (2019).

[105] R. Blankenbecler, D. J. Scalapino, and R. L. Sugar, *Monte Carlo calculations of coupled boson-fermion systems. I*, Phys. Rev. D **24**, 2278 (1981).

[106] A. Toschi, A. A. Katanin, and K. Held, *Dynamical vertex approximation: A step beyond dynamical mean-field theory*, Phys. Rev. B **75**, 045118 (2007).

[107] G. Rohringer, H. Hafermann, A. Toschi, A. A. Katanin, A. E. Antipov, M. I. Katsnelson, A. I. Lichtenstein, A. N. Rubtsov, and K. Held, *Diagrammatic routes to nonlocal correlations beyond dynamical mean field theory*, Rev. Mod. Phys. **90**, 025003 (2018).

[108] T. Maier, M. Jarrell, T. Pruschke, and M. H. Hettler, *Quantum cluster theories*, Rev. Mod. Phys. **77**, 1027 (2005).

[109] J. Kaufmann, C. Eckhardt, M. Pickem, M. Kitatani, A. Kauch, and K. Held, *Self-consistent ab initio $D\Gamma A$ approach* (2020), arXiv:2010.03938 [cond-mat.str-el].

[110] A. A. Katanin, A. Toschi, and K. Held, *Comparing pertinent effects of antiferromagnetic fluctuations in the two- and three-dimensional Hubbard model*, Phys. Rev. B **80**, 075104 (2009).

[111] G. Rohringer and A. Toschi, *Impact of nonlocal correlations over different energy scales: A dynamical vertex approximation study*, Phys. Rev. B **94**, 125144 (2016).

[112] D. L. Bergman, C. Wu, and L. Balents, *Band touching from real-space topology in frustrated hopping models*, Phys. Rev. B **78**, 125104 (2008).

[113] E. Gull, A. J. Millis, A. I. Lichtenstein, A. N. Rubtsov, M. Troyer, and P. Werner, *Continuous-time Monte Carlo methods for quantum impurity models*, Rev. Mod. Phys. **83**, 349 (2011).

[114] M. Wallerberger, A. Hausoel, P. Gunacker, A. Kowalski, N. Parragh, F. Goth, K. Held, and G. Sangiovanni, *w2dynamics: Local one- and two-particle quantities from dynamical mean field theory*, Comput. Phys. Commun. **235**, 388 (2019).

[115] J. Kaufmann, P. Gunacker, A. Kowalski, G. Sangiovanni, and K. Held, *Symmetric improved estimators for continuous-time quantum Monte Carlo*, Phys. Rev. B **100**, 075119 (2019).

[116] P. Gunacker, M. Wallerberger, E. Gull, A. Hausoel, G. Sangiovanni, and K. Held, *Continuous-time quantum Monte Carlo using worm sampling*, Phys. Rev. B **92**, 155102 (2015).

[117] A. Galler, P. Thunström, P. Gunacker, J. M. Tomczak, and K. Held, *Ab initio dynamical vertex approximation*, Phys. Rev. B **95**, 115107 (2017).

[118] D. Hirschmeier, H. Hafermann, and A. I. Lichtenstein, *Multiband dual fermion approach to quantum criticality in the Hubbard honeycomb lattice*, Phys. Rev. B **97**, 115150 (2018).

[119] E. Y. Loh, J. E. Gubernatis, R. T. Scalettar, S. R. White, D. J. Scalapino, and R. L. Sugar, *Sign problem in the numerical simulation of many-electron systems*, Phys. Rev. B **41**, 9301 (1990).

[120] V. I. Iglovikov, E. Khatami, and R. T. Scalettar, *Geometry dependence of the sign problem in quantum Monte Carlo simulations*, Phys. Rev. B **92**, 045110 (2015).

[121] All analytic continuations are done using the maximum entropy method as implemented in ana-cont [127].

[122] J. Graf, G.-H. Gweon, K. McElroy, S. Y. Zhou, C. Jozwiak, E. Rotenberg, A. Bill, T. Sasagawa, H. Eisaki, S. Uchida, H. Takagi, D.-H. Lee, and A. Lanzara, *Universal High Energy Anomaly in the Angle-Resolved Photoemission Spectra of High Temperature Superconductors: Possible Evidence of Spinon and Holon Branches*, Phys. Rev. Lett. **98**, 067004 (2007).

[123] Due to the topology of the lattice with three sites in the unit cell and a triangular Bravais lattice, one might expect e.g. 120° orientations of the spins on neighboring sites. However, the $-120°$ orientation is symmetrically equivalent, so that a prevalence toward such spin-orientation translates to a negative (albeit incomplete) $\langle S_z^j S_z^l \rangle$ correlation.

[124] M. Punk, D. Chowdhury, and S. Sachdev, *Topological excitations and the dynamic structure factor of spin liquids on the kagome lattice*, Nature Physics **10**, 289 (2014).

[125] N. E. Sherman and R. R. P. Singh, *Structure factors of the kagome-lattice Heisenberg antiferromagnets at finite temperatures*, Phys. Rev. B **97**, 014423 (2018).

[126] D. Geffroy, J. Kaufmann, A. Hariki, P. Gunacker, A. Hausoel, and J. Kuneš, *Collective Modes in Excitonic Magnets: Dynamical Mean-Field Study*, Phys. Rev. Lett. **122**, 127601 (2019).

[127] J. Kaufmann, *ana_cont: Package for analytic continuation of many-body Green's functions*, `https://github.com/josefkaufmann/ana_cont` (2020).

[128] M. Jarrell and J. Gubernatis, *Bayesian inference and the analytic continuation of imaginary-time quantum Monte Carlo data*, Physics Reports **269**, 133 (1996).

[129] M. Udagawa and Y. Motome, *Chirality-Driven Mass Enhancement in the Kagome Hubbard Model*, Phys. Rev. Lett. **104**, 106409 (2010).

[130] T. Kita, T. Ohashi, and N. Kawakami, *Field-induced Mott transition in kagome lattice Hubbard model*, Phys. Rev. B **87**, 155119 (2013).

[131] A. Ralko, F. Mila, and I. Rousochatzakis, *Microscopic theory of the nearest-neighbor valence bond sector of the spin-$\frac{1}{2}$ kagome antiferromagnet*, Phys. Rev. B **97**, 104401 (2018).

[132] L. Messio, O. Cépas, and C. Lhuillier, *Schwinger-boson approach to the kagome antiferromagnet with Dzyaloshinskii–Moriya interactions: phase diagram and dynamical structure factors*, Phys. Rev. B **81**, 064428 (2010).

[133] T. Dodds, S. Bhattacharjee, and Y. B. Kim, *Quantum spin liquids in the absence of spin-rotation symmetry: Application to herbertsmithite*, Phys. Rev. B **88**, 224413 (2013).

[134] J. C. Halimeh and M. Punk, *Spin structure factors of chiral quantum spin liquids on the kagome lattice*, Phys. Rev. B **94**, 104413 (2016).

[135] J. C. Halimeh and R. R. P. Singh, *Rapid filling of the spin gap with temperature in the Schwinger-boson mean-field theory of the antiferromagnetic Heisenberg kagome model*, Phys. Rev. B **99**, 155151 (2019).

[136] A. M. Läuchli and C. Lhuillier, *Dynamical Correlations of the Kagome $S = 1/2$ Heisenberg Quantum Antiferromagnet* (2009), arXiv:0901.1065 [cond-mat.str-el].

[137] T. F. Seman, C.-C. Chen, R. R. P. Singh, and M. van Veenendaal, *The many faces of quantum kagome materials: Interplay of further-neighbour exchange and Dzyaloshinskii-Moriya interaction* (2015), arXiv:1508.01523 [cond-mat.str-el].

[138] W. Zhu, S. Gong, and D. N. Sheng, *Identifying spinon excitations from dynamic structure factor of spin-1/2 Heisenberg antiferromagnet on the Kagome lattice*, Proc. Natl. Acad. Sci. **116**, 5437 (2019).

[139] L. Messio, C. Lhuillier, and G. Misguich, *Lattice symmetries and regular magnetic orders in classical frustrated antiferromagnets*, Phys. Rev. B **83**, 184401 (2011).

[140] J. D. Hunter, *Matplotlib: A 2D graphics environment*, Computing in Science & Engineering **9**, 90 (2007).